Chapter 1

Introduction

In this chapter, I will first explain several basic concepts about glasses and metallic glasses. Then I will give a brief summary on the history of metallic glass research and the motivation for this thesis. In the third section, I will go over the thermodynamics and kinetics related to metallic glass formation, including D.R. Uhlmann's TTT (Time-Temperature-Transformation) analysis. In the last section, I will review several frequently used criteria for bulk metallic glass development which have been proposed in the past years.

1.1 Basic concepts about glasses and metallic glasses

1.1.1 Glass and glass transition

A *glass* is a disordered (or amorphous) solid which does not possess the long range periodicity as present in a typical *crystal.* As continuous refinement of crystal grains is being achieved these days, the boundary between a glass and a nanocrystalline solid with very fine grains is getting blurred. For most practical purposes, however, if no long range order can be detected beyond a 1-2 nm scale, a solid can be called a glass.

It should be noted that the definition of a glass is made only based on its disordered structure[†], regardless of its chemical composition. In fact, a glass may chemically have any of the available types of bonding: metallic, covalent, ionic, hydrogen and van der

[†] Some researchers prefer not to use the word 'structure' on a glass. However, in this thesis I will still use the word, considering the existence of short range ordering in a glass.

Waals. Here in this thesis, we mainly focus on glasses with metallic bonding, i.e., *metallic glasses*.

Due to the existence of crystalline counterparts which have lower free energy, a glass is not a thermodynamically stable form of solids even though it may possess excellent metastability [1] (e.g., silicate glasses). For this reason, a glass always has a tendency to transform into more stable crystalline forms by a *crystallization* process. The crystallization may be induced by heating or mechanical deformation, and may proceed either rapidly or slowly as we will discuss in more detail in the following sections.

Upon continuous heating, a glass with good metastability undergoes a *glass transition* before crystallization occurs. This glass transition is manifested by a rather rapid increase in both heat capacity (C_p) and coefficient of thermal expansion (CTE)[†]. At the same time, the sample's mechanical response to external stresses also changes rapidly from solid-like to liquid-like as described by a significant drop in viscosity (η) (typically by several orders of magnitude). Because this transition spans a range of temperatures, there are different ways to define a characteristic temperature for this transition, usually called *glass transition temperature* (T_g) [2]. The definition of T_g adopted in this thesis is the onset temperature of the C_p increase upon heating at a constant rate of 0.33 K/s. Another frequently used definition of T_g is the temperature at which the equilibrium viscosity of the heated glass becomes 10^{13} poise (i.e., 10^{12} Pa s). This specific value of viscosity was chosen rather arbitrarily to distinguish a viscous liquid from a solid. Whichever definition one uses, the T_g should always be regarded as the boundary between the pre-transition

[†] Other second order derivatives of energy such as compressibility and elastic modulli also experience an abrupt change (either an increase or decrease) during the glass transition.

and the post-transition states of the glass. Due to its liquid-like feature and its thermodynamic metastability, a glass in the post-transition state is also called an *undercooled liquid*.

Although the above description of glass transition is based on the continuous heating of a glass, the glass transition also takes place during the continuous cooling of a liquid, if no crystallization interferes. Moreover, the glass transition is roughly reversible upon cooling and heating if the cooling rate ($\left|\dot{T}^C\right|$) is about equal to the heating rate ($\dot{T}^H$) in magnitude. If $\dot{T}^H >> \left|\dot{T}^C\right|$, however, the glass transition occurs at a higher temperature during heating (T_g^H) than during cooling (T_g^C). On the other hand, if $\dot{T}^H << \left|\dot{T}^C\right|$, the glass transition appears at a lower temperature during heating than during cooling. In addition, the larger the mismatch in the two rates, the more obvious the discrepancy between T_g^H and T_g^C. These phenomena are all related to the structural relaxation of the glass which is a kinetic process. In the former case above ($\dot{T}^H >> \left|\dot{T}^C\right|$), the glass does not have as much time as during cooling to relax when it passes through T_g^C during heating and therefore, it retains its solid configuration to higher temperature until it reaches T_g^H. In the latter case ($\dot{T}^H << \left|\dot{T}^C\right|$), the glass has more time to relax during heating (than during cooling) so that it readily gives up its solid configuration at a lower temperature than T_g^C.

1.1.2 Glass formation and glass-forming ability

Glasses, including metallic glasses, can be formed through different routes starting from different initial states [2]. Perhaps most frequently, however, glasses are formed through the continuous cooling of liquids from above their thermodynamic melting temperature (T_m) to below their glass transition temperature T_g.

In order to eventually form a glass upon continuous cooling, a liquid has to 'successfully' suppress crystallization. Although crystallization is favored by thermodynamics below the melting temperature, it is subject to the control of the kinetics of crystal nucleation and growth such that it requires a certain amount of time to proceed. Apparently, if a liquid were cooled instantaneously from T_m to T_g using an infinitely high cooling rate, there would be no time for crystallization to proceed and the liquid would be directly frozen into a glass by going through a glass transition around T_g. In actual cases, however, the cooling rate required to form a practical glass does not need to be infinitely high because the crystallization does not have to be completely restrained. As long as the crystallized volume fraction in the resulted solid is beyond the detection limit of the characterization instruments, the resulted solid is considered as a glass for practical purposes. This limiting crystallization volume fraction, f_c, is often taken as 10^{-6} (a value chosen rather arbitrarily) for all practical glasses. Hence, corresponding to this f_c, there is a finite critical value of the cooling rate which is normally called the *critical cooling rate* R_c for each liquid. A liquid can form a glass if and only if the actual cooling rate is higher than its R_c. The critical cooling rate depends on the thermodynamics and kinetics of crystallization (as we will discuss in more detail in Section 1.3) and may vary a lot

from one liquid to another. For example, the liquid of multi-component $Zr_{41.2}Ti_{13.8}Cu_{12.5}Ni_{10}Be_{22.5}$[†] alloy has an R_c around 1.4 K/s [3], while the liquid of binary $Zr_{65}Be_{35}$ alloy has an R_c around 10^7 K/s [4]. The critical cooling rate is the ultimate judgment factor for the glass-forming ability (GFA) of a liquid. Obviously, a liquid with a lower R_c has a higher GFA.

There are many different methods to cool a liquid into a glass. As for metallic glasses, the available cooling methods include melt spinning, splat quenching, metal (usually copper) mold casting, water quenching and others [5], among which copper mold casting is the one most heavily utilized in this thesis.

Consider the heat transfer during the cooling of a liquid alloy within a copper mold. If the liquid solidifies into a glass, then no latent heat due to crystallization needs to be considered. If one dimension (we call it thickness, l) of the slot holding the liquid is significantly lower than the other two, the problem can be described by the one dimensional Fourier heat flow equation along the thickness direction:

$$\frac{\partial T}{\partial t} = \kappa \frac{\partial^2 T}{\partial x^2} \tag{1.1}$$

where x is spatial coordinate ($0 \le x \le l$), t is time, $T = T(x,t)$ is temperature, and κ is the thermal diffusivity of the liquid alloy. The initial condition is $T(x,0) = T_l$ where T_l is the liquidus temperature of the alloy. The boundary conditions are $T(0,t) = T(x,t) = T_r$ where T_r is the room temperature (we treat the copper mold as a heat reservoir and

[†] All the compositions in this thesis are given in atomic percentage.

neglect the temperature change in the mold). The exact solution to this problem can be easily found:

$$T(x,t) = T_r + \frac{4(T_l - T_r)}{\pi}\sum_{n=1}^{\infty}\frac{1}{2n-1}\sin[\frac{(2n-1)\pi}{l}x]\exp[-(2n-1)^2\pi^2\frac{\kappa t}{l^2}]. \qquad (1.2)$$

We would like to know how fast the center ($x = l/2$) of the liquid is cooled down to T_g since this determines whether crystallization would occur. Using the first order approximation to Eq. (1.2), we get the time τ it takes the center to reach T_g:

$$\tau = \frac{l^2}{\pi^2\kappa}\ln(\frac{4}{\pi}\frac{T_l - T_r}{T_g - T_r}) \qquad (1.3)$$

Therefore, the cooling rate at the center averaged in the temperature interval between T_l and T_g is:

$$R = \frac{T_l - T_g}{\tau} = \frac{\pi^2\kappa}{l^2}(T_l - T_g)/\ln(\frac{4}{\pi}\frac{T_l - T_r}{T_g - T_r}) \qquad (1.4)$$

It can be seen that the cooling rate depends on several parameters: glass transition temperature T_g , liquidus temperature T_l, thermal diffusivity κ, and sample thickness l. For a given alloy, R is inversely proportional to the square of l. In order to successfully suppress crystallization, R has to be larger than the critical cooling rate R_c of the alloy liquid, which requires that l be smaller than a critical value (usually called the *critical casting thickness*) l_c. If the contribution of other factors, i.e, T_g, T_l, and κ, to the cooling rate R does not vary much from one alloy to another, according to Eq. (1.4), the critical casting thickness of the alloys can then be used to distinguish their glass-forming ability.

Eq. (1.4) can be used to calculate either one of the critical cooling rate and the critical casting thickness if the other is known. For extremely good metallic glass formers like $Pd_{40}Cu_{30}Ni_{10}P_{20}$ [6] and $Zr_{41.2}Ti_{13.8}Cu_{12.5}Ni_{10}Be_{22.5}$ [3], it is very easy to measure the critical cooling rate (e.g., via DSC—Differential Scanning Calorimetry), but difficult to directly measure the critical casting thickness by repeated castings[†] of large quantities of materials. For moderately good metallic glass formers like the ones developed in this thesis, $Ni_{59.35}Nb_{34.45}Sn_{6.2}$ [7], $Cu_{64}Zr_{36}$ [8], $Cu_{46}Zr_{54}$ and $Cu_{46}Zr_{42}Al_7Y_5$ [9], and $Ni_{40}Cu_5Ti_{16.5}Zr_{28.5}Al_{10}$ [10] to name but a few, it is easy to find out the critical casting thickness via repeated castings, but difficult to directly measure the critical cooling rate using DSC.

1.2 History of metallic glass research and motivation for this thesis

The production of an amorphous flake (~10 μm in thickness) by rapid cooling of the molten $Au_{75}Si_{25}$ alloy in 1960 [11] is generally considered the beginning of the era of metallic glasses, even though prior to that, disordered metallic materials had been made through other routes such as vapor condensation on substrates at liquid helium temperature [12]. In the long period that followed until a breakthrough occurred in the late 1980's and early 1990's with the discovery of several multi-component metallic glasses with very low critical cooling rates, the formation of metallic glasses in many simple alloy systems (mainly binary and ternary systems) was discovered and the properties of the resulted metallic glasses were studied (see Ref. [13-18] for examples of these early works). Many of these studies showed that metallic glasses possess several

[†] To find out the critical casting thickness, multiple values of sample thickness have to be tested; each value requires a casting and subsequent inspection with characterization instruments like an X-ray diffractometor.

unique properties that are superior to the conventional crystalline metals and alloys, such as very high strength (close to theoretical limits for metals and alloys), high elastic strain limit, high hardness, high corrosion resistance, and very good soft magnetism (with very low coercivity and low hysteretic losses). These properties indicated that metallic glasses could be much better than conventional metals and alloys in many structural and functional applications. Nevertheless, the real applications of metallic glasses in most cases could not be realized because of the barriers in the formation of these materials. The critical cooling rates of these early metallic glasses were so high (on the order of 10^5-10^7 K/s) that the samples had to be very small (typically tens of microns or less) in at least one dimension in order to form a glassy structure and that special techniques (e.g., melt spinning) had to be utilized to acquire such high cooling rates. A logical way to solve these problems would be to find some new metallic glasses with low critical cooling rates which can be formed into bulk samples[†]. In 1984, one such alloy, $Pd_{40}Ni_{40}P_{20}$, was found to form 10 mm thick glassy samples using a very low cooling rate (<1 K/s) [19]. Unfortunately, this alloy could not be used as a practical metallic glass because it was based on palladium, a very expensive component.

A breakthrough came in the late 1980s and early 1990s when several metallic glasses based on practical elements with very low critical cooling rates were discovered (e.g., $Zr_{41.2}Ti_{13.8}Cu_{12.5}Ni_{10}Be_{22.5}$ [20] and $La_{55}Al_{25}Ni_{20}$ [21]). These alloys could easily be fabricated into bulk glassy samples by the regular mold casting method or water quenching. On one hand, the discovery of these bulk metallic glasses (BMGs) significantly enhanced the promise of metallic glasses as practical materials. Particularly,

[†] The boundary between 'bulk' and 'thin' is generally taken as 1 mm (in the smallest dimension) by researchers in this area.

the Zr-based BMGs have already been fabricated into commercial parts and articles for packaging, medical, and sporting purposes. On the other hand, the discovery of these BMGs also made it possible to perform fundamental studies on metallic glasses and their undercooled liquids that had been forbidden by the formerly limited sample size or limited resistance to crystallization.

However, there are still limitations to these early BMGs. For example, their glass transition temperatures are usually quite low, which prevent them from high temperature applications, and their material costs are relatively high, leaving space for further reduction. Meanwhile, the limited number of BMGs prevents a complete understanding of metallic glasses as a whole category of solids. It is therefore necessary to develop more BMGs, from either a technological or scientific point of view. As part of a unified endeavor in the academic community, this thesis research is aimed at facilitating the variety within the family of BMG alloys.

BMGs based on certain late transition metals (e.g., Fe, Co, Ni, Cu) have many potential advantages over those based on early transition metals (e.g., Zr, La). These advantages include even higher strength and elastic modulii, and lower material costs, to name but a few that are highly preferable for broad applications of BMGs as engineering materials. Nevertheless, these ordinary-late-transition-metal-based BMGs generally have quite limited glass-forming ability. In particular, for the Ni-based and Cu-based alloys reported prior to this research, the maximum casting thickness allowed to retain their amorphous structures is only ~2 mm (or lower) and ~5 mm (or lower), respectively [22-25]. In this

thesis, attention is focused on the development of novel Ni- and Cu-based BMGs with higher glass-forming ability.

1.3 Thermodynamics and kinetics related to glass formation and TTT (Time-Transformation-Temperature) diagram

1.3.1 Thermodynamics of an undercooled liquid

A liquid (l) has the same Gibbs free energy (G) as its crystal (x), i.e., $G_l = G_x$ (or $\Delta G_m = G_l - G_x = 0$) at the melting temperature T_m. Also at T_m, the liquid has more entropy (S) than its crystal by the amount of $\Delta S_m = S_l - S_x = \Delta H_m / T_m$, where ΔH_m is the heat (i.e., enthalpy) of fusion. When temperature T is below T_m, the liquid is undercooled and has a higher Gibbs free energy than the crystal. The energy difference $\Delta G = \Delta G_m + \int_{T_m}^{T} (-\Delta S) dT = -\int_{T_m}^{T} \Delta S dT$ acts as the driving force for crystallization of the undercooled liquid. The entropy difference between the two states is described as $\Delta S = \Delta S_m + \int_{T_m}^{T} \frac{\Delta C_p}{T} dT$, where $\Delta C_p = C_{p,l} - C_{p,x}$ (>0) is the heat capacity difference between the liquid and the crystal. Since the liquid has a higher heat capacity, it loses its entropy faster than the crystal upon cooling. As the temperature drops continuously, there would appear a point at which the entropy of the liquid became equal to that of the crystal. This tendency was first pointed out by Kauzmann [26] and therefore, it is now known as the 'Kauzmann Paradox.' The isentropic point is called Kauzmann temperature, T_K. The Kauzmann temperature is considered as the limit to which a liquid can be cooled with the

argument that a liquid can't have lower entropy than its crystal[†]. Therefore, before reaching T_K, either glass transition or crystallization has to occur in order to terminate the liquid state. In either case, the heat capacity experiences an abrupt drop.

In principle, both $C_{p,l}$ (between T_m and T_g) and $C_{p,x}$ can be measured experimentally using calorimetric method [27] or ESL (ElectroStatic Levitation) technique [28], although the measurement of $C_{p,l}$ requires high resistance of the undercooled liquid to crystallization. In fact, this has been done on some extremely good metallic glasses (e.g., $Zr_{41.2}Ti_{13.8}Cu_{12.5}Ni_{10}Be_{22.5}$ [27, 28]). The melting temperature T_m and the heat of fusion ΔH_m can easily be measured using high temperature calorimetry. With the $C_{p,l}$, $C_{p,x}$ (and hence ΔC_p), T_m and ΔH_m known, the Gibbs free energy difference between the undercooled liquid and the crystal as a function of temperature can be calculated as follows:

$$\Delta G = \frac{\Delta H_m}{T_m}(T_m - T) - \int_{T_m}^{T} dT' \int_{T_m}^{T'} \frac{\Delta C_p(T'')}{T''} dT'' \qquad (1.5)$$

It should be noted that the thermodynamic parameters are well defined functions of temperature T and pressure P, and do not depend on the cooling rates or the heating rates exploited in their experimental measurements.

[†] This would happen if the liquid were cooled to below T_K.

1.3.2 Kinetics of an undercooled liquid

Viscosity η is perhaps the most important kinetic parameter of an undercooled liquid since other kinetic parameters can usually be obtained from η. For example, relaxation times, τ, including shear stress (Maxwell) relaxation time and internal viscosity equilibration time, are directly proportional to η, although the proportion coefficient may be different for different times [29]. Diffusivity D is inversely proportional to η as formulated by the Stokes-Einstein equation:

$$D = \frac{k_B T}{3\pi l \eta} \tag{1.6}$$

where k_B is the Boltzmann constant and l the average atomic diameter. Therefore, it is a key issue to study the viscosity of an undercooled liquid as a function of temperature.

There are several models to describe the experimentally measured temperature dependence of the equilibrium viscosity (fully relaxed) of an undercooled liquid. Perhaps the two most frequently used are the Vogel-Fulcher-Tamman (VFT) model [2, 30-32] and the free volume model [33].

In the VFT model (slightly modified by C. A. Angell [2]), the viscosity is expressed as:

$$\eta(T) = \eta_0 \exp(\frac{DT_0}{T - T_0}) \tag{1.7}$$

where η_0, D and T_0 are three constants from fitting of experimental data. Physically, η_0 refers to the viscosity extrapolated to the infinite temperature, D is a 'strength' parameter

(the higher D, the stronger the liquid; see below for more details), and T_0 is an extrapolated temperature (usually called the VFT temperature) at which the viscosity would diverge.

Experimental data have shown that most glass-forming liquids show a deviation from Arrhenius behavior (corresponding to T_0 =0 and $D=\infty$ in the VFT model) in their viscosity. As can be seen in Fig 1.1 (reproduced from [2]), the $\log_{10}\eta$ vs. T_g/T plots of the many glass-forming liquids are curved rather than linear (corresponding to Arrhenius behavior). The higher the curvature, the more the liquid deviates from Arrhenius behavior, or in more fashionable terms, the more 'fragile' or less 'strong' is the liquid. If η_0 and T_0 are fixed in the VFT model above, a higher D will correspond to a lower curvature (i.e., a strong liquid). Hence, the D is normally known as the strength parameter of a liquid. Another way to describe the deviation from the Arrhenius behavior [34] is the slope of the $\log_{10}\eta$ vs. T_g/T plot at the glass transition temperature T_g

$$m=\left.\frac{d\log_{10}\eta}{dT_g/T}\right|_{T_g}=0.434\frac{DT_gT_0}{(T_g-T_0)^2} \tag{1.8}$$

The larger the slope m, the more fragile is the liquid. Therefore, m is called the 'fragility' of the liquid. Usually, fragile liquids have $m\geq 100$ and strong liquids have m in the range of 16~30 [34]. For some good[†] metallic glasses such as Zr- and Pd-based BMGs, the fragility typically values from 32 to 66 [35], while for some poor metallic glass-formers like Al-based alloys, the fragility may be higher than 200 [36]. Due to its purely kinetic

[†] in terms of glass-forming ability

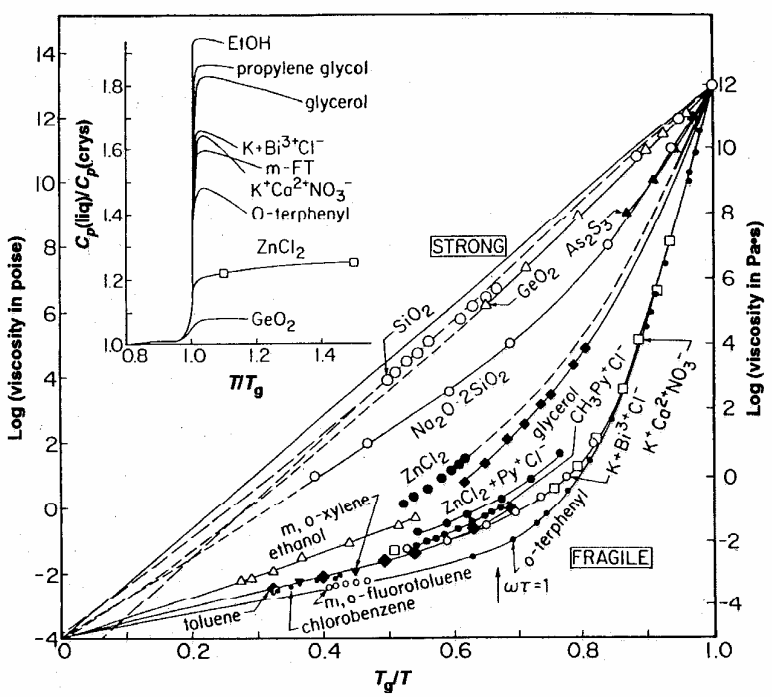

Fig 1.1 Plots of viscosity data scaled by values of T_g for different glass-forming liquids. The inset is the heat capacity change during the glass transition for these liquids (reproduced after Ref. [2]).

nature, however, the fagility parameter is not expected to fully describe the glass-forming ability of a liquid as we will see in the next section depends on both thermodynamics and kinetics of the undercooled liquid.

While the viscosity of some metallic glass forming liquids such as $Pd_{40}Cu_{30}Ni_{10}P_{20}$ [37] can be described well by the VFT model, others (e.g., $Zr_{41.2}Ti_{13.8}Cu_{12.5}Ni_{10}Be_{22.5}$ [29]) require another: the free volume model. In this model, the viscosity is described as:

$$\eta = \frac{h}{v_m}\exp(\frac{bv_m}{v_f}) \tag{1.9}$$

where v_m and v_f are the molecular (atomic in the case of metallic glass) volume and the mean free volume per molecule, respectively, and h is Planck's constant. This model assumes that the change in viscosity of a liquid is caused by the reduction (upon cooling) or expansion (upon heating) of the mean free volume v_f. The temperature dependence of the free volume is fitted as follows:

$$v_f = c_1[T - T_0 + \sqrt{(T - T_0)^2 + c_2 T}] \tag{1.10}$$

where c_1, c_2 and T_0 (all positive) are three fitting parameters. Eq. (1.10) prevents the divergence of viscosity at a finite temperature. At high temperature, $v_f \sim 2c_1(T - T_0)$ and at low temperature, $v_f \sim c_1 T$. Therefore, this model describes a transition from VFT behavior (at high T) to Arrhenius behavior (at low T) that has been observed in $Zr_{41.2}Ti_{13.8}Cu_{12.5}Ni_{10}Be_{22.5}$ [29].

It should be noted that the above models are only for equilibrium viscosity. The instantaneous viscosity at a temperature (especially around the glass transition temperature) may be quite different from the equilibrium viscosity, depending on the history (initial condition), time, and temperature. For example, if a liquid is maintained at a constant temperature, its viscosity tends to evolve with time towards the equilibrium value determined by the above models. This is a kinetic relaxation process which can usually be described by a first-order reaction law as follows:

$$\left.\frac{\partial \eta}{\partial t}\right|_T = k(\eta_\infty - \eta) \tag{1.11}$$

where k is the rate constant (the inverse of relaxation time τ) and η_∞ is the equilibrium viscosity (corresponding to $t = \infty$) at the temperature T. Both k and η_∞ depend on temperature only. Therefore, the instantaneous viscosity during this isothermal relaxation process can be derived from Eq. (1.11) as:

$$\eta(t) = \eta_\infty + (\eta_0 - \eta_\infty)\exp(-kt) \tag{1.12}$$

where η_0 is the initial viscosity at $t = 0$. It can be seen that the time evolution of the instantaneous viscosity takes an exponential form. Also note $k = 1/\tau = G/\eta_\infty$ where G is the shear modulus at temperature T for the internal relaxation process (which may be different from the shear modulus for external stress relaxation within the Maxwell's model of viscoelasticity [29]).

1.3.3 Classical theory for crystal nucleation and growth from an undercooled liquid and TTT diagram

When a liquid is cooled below its melting temperature T_m, crystallization tends to occur by crystal nucleation and growth.

For a crystal to nucleate, the Gibbs free energy difference between the liquid and the crystal acts as the driving force. On the other hand, nucleation involves the creation of an interface between the two phases which tends to increase the system energy. Assuming a spherical shape of the nucleus and a homogeneous[†] manner of the nucleation process (the other type, heterogeneous nucleation, will be discussed in Chapter 4), the total energy change caused by the formation of the nucleus is:

$$\Delta E = 4\pi r^2 \sigma - \frac{4}{3}\pi r^3 \Delta G \tag{1.13}$$

where r, σ and ΔG are the radius of the nucleus, the interfacial energy per area, and the Gibbs free energy difference per volume between the two phases, respectively. It can been seen from Fig 1.2 that there is a maximum for ΔE corresponding to a critical nucleus radius r_c. If a nucleus has a radius lower than r_c, it can't grow spontaneously because that would cause the system energy to increase. In contrast, a nucleus with a radius larger than r_c can grow spontaneously because that will cause the system energy

[†] Homogeneous nucleation means there are no extrinsic nucleating agents.

to drop. By setting $\left.\frac{d\Delta E}{dr}\right|_{r_c} = 0$, one can calculate the critical nucleus radius r_c and its corresponding critical energy barrier ΔE_c:

$$\begin{aligned} r_c &= \frac{2\sigma}{\Delta G} \\ \Delta E_c &= \frac{16\pi}{3}\frac{\sigma^3}{\Delta G^2} \end{aligned} \tag{1.14}$$

The classical theory of nucleation (e.g., Ref. [38]) depicts the nucleation rate[†], I_v, as the product of one kinetic term and one thermodynamic term as follows:

$$I_v = \frac{A_v}{\eta}\exp(-\frac{\Delta E_c}{k_B T}) = \frac{A_v}{\eta}\exp(-\frac{16\pi\sigma^3}{3k_B T\Delta G^2}) \tag{1.15}$$

where A_v is a constant of the order of 10^{32} Pa s/(m^3 s) for homogeneous nucleation, η is the viscosity, and k_B is the Boltzmann constant. The viscosity has a temperature dependence as described by the kinetic models in Section 1.3.2. Here, we choose to use the VFT model (i.e., $\eta(T) = \eta_0 \exp(\frac{DT_0}{T - T_0})$). The Gibbs free energy difference per volume between the liquid and the crystal (i.e., ΔG), also has a temperature dependence as given by Eq. (1.5) in Section 1.3.1. For simplicity, we take a first-order approximation (i.e., $\Delta G = \Delta S_m (T_m - T)$; ΔS_m is the entropy of fusion per volume).

The classical theory describes the crystal growth rate[‡] also using the product of one

[†] defined by the number of critical nuclei that are formed within a unit volume per second
[‡] defined by the derivative of the crystal grain (nucleus) radius with respect to time, thus in units of m/s

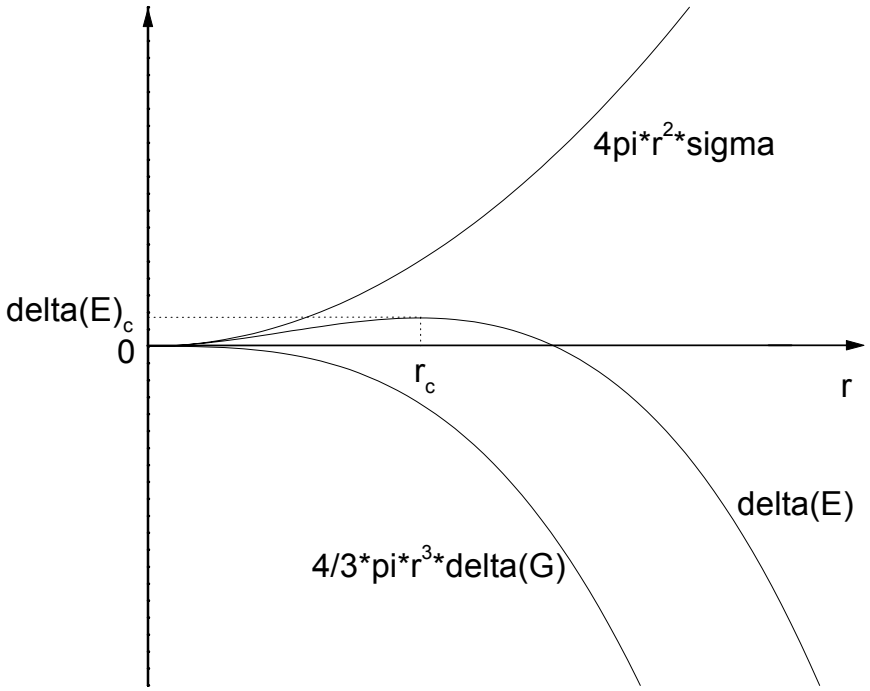

Fig 1.2 Plots of the three terms in Eq. (1.13) vs. nucleus radius *r*.

kinetic term and one thermodynamic term as follows:

$$u = \frac{k_B T}{3\pi l^2 \eta}[1 - \exp(-\frac{n\Delta G}{k_B T})] \tag{1.16}$$

where l is the average atomic diameter and n is the average atomic volume. The first (kinetic) term was originally expressed using atomic diffusivity. The form of Eq. (1.16) has utilized the Stokes-Einstein relation between the diffusivity and the viscosity which was given by Eq. (1.6) in Section 1.3.2.

For the best metallic glass former $Pd_{40}Cu_{30}Ni_{10}P_{20}$, the constant parameters have been determined to be: $\eta_0 = 9.34\times10^{-3}$ Pa s, $D = 9.25$, $T_0 = 447$ K [37], $T_m = 823$ K, $\Delta S_m = 9.344\times10^5$ J/(m^3 K) [39], $\sigma = 0.067$ J/m^2, $A_v = 4.4\times10^{31}$ Pa s/(m^3 s), $n = 1.52\times10^{-29}$ m^3, and $l = 3.1\times10^{-10}$ m [40]. Using these parameters, one can plot both the nucleation rate and the crystal grow rate as a function of temperature for this alloy as shown in Fig1.3.

From Fig1.3, one can see that both I_v and u exhibit a maximum below T_m. Further, the maximum of the nucleation rate occurs at a lower temperature than that of the growth rate. This is generally true for any liquid. The physical reason for this is that the influence of the viscosity factor (the kinetic term) to the nucleation rate is not as significant as to the growth rate. Since the viscosity increases as temperature decreases from T_m, it hinders the increase in the growth rate more effectively than it does the increase in the nucleation rate. Therefore, the increase in the growth rate is stopped earlier by the viscosity than the

increase in the nucleation rate, which results in a higher peak temperature for the growth rate than for the nucleation rate.

Having known I_v and u, one can calculate the volume fraction, f, of the crystallized part of the undercooled liquid as a function of time at an early† stage of crystallization by an iterated integral as follows:

$$f = \int_0^t I_v(t')dt' \frac{4}{3}\pi[\int_{t'}^t u(t'')dt'']^3 \tag{1.17}$$

where t' and t'' are the two time coordinates for the nucleation and for the growth, respectively.

For an isothermal crystallization process with the viscosity equilibrated (no relaxation with time), I_v and u are independent of time. Then, Eq. (1.17) can be simplified as:

$$f = \frac{4}{3}\pi I_v u^3 \int_0^t dt'(t-t')^3 = \frac{1}{3}\pi I_v u^3 t^4 \tag{1.18}$$

Therefore, the time required to crystallize a certain volume fraction of the liquid is given by:

$$t = (\frac{3f}{\pi I_v u^3})^{1/4} \tag{1.19}$$

In Section 1.1.2, we introduced a critical value of f, i.e., $f_c = 10^{-6}$ as the boundary

† which means that the growing nuclei are not affected by each other and that the liquid matrix is not changed much by crystallization so that Eq. (1.15) and (1.16) can apply.

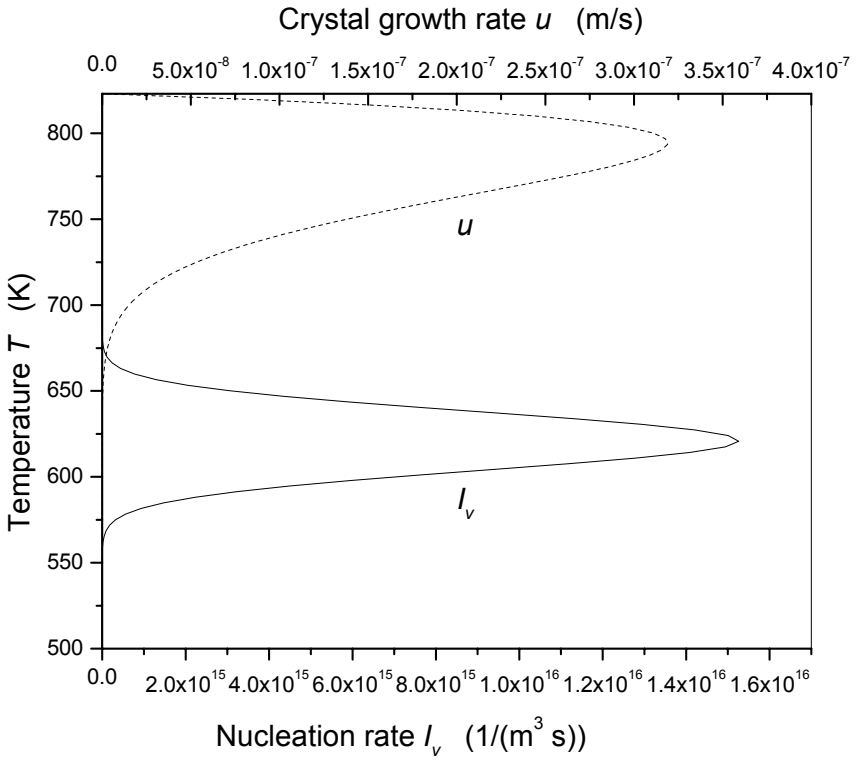

Fig 1.3 Nucleation rate I_v and crystal growth rate u as a function of temperature for the BMG alloy $Pd_{40}Cu_{30}Ni_{10}P_{20}$.

between 'crystallized' and 'not crystallized' for practical glasses. Here, we can calculate the time required to crystallize an f_c fraction of the liquid at different temperatures using Eq. (1.19). We still use the above $Pd_{40}Cu_{30}Ni_{10}P_{20}$ as a sample system. The calculation result for this alloy is plotted in Fig 1.4. This certain type of plot as in Fig 1.4 is called Uhlmann's TTT (Time-Temperature-Transformation) diagram since Uhlmann first utilized this to analyze the glass-forming ability of different substances [41].

From Fig 1.4 one can see that a TTT diagram has a C shape with a nose at an intermediate temperature between the T_m (we use liquidus temperature T_{liq} for an alloy) and T_g. Crystallization (of a small volume fraction, here $f_c = 10^{-6}$) takes the shortest incubation time, t_n, at the nose temperature T_n. Here, from Fig 1.4, we find $t_n = 32$ s, and $T_n = 671$ K. According to early analysis by Uhlmann [41], the dotted line passing through the nose of the TTT curve in Fig 1.4 gives the critical cooling rate $R_c^{TTT-iso}$ † required to bypass significant crystallization and form a practical glass:

$$R_c^{TTT-iso} = \frac{T_m - T_n}{t_n} \tag{1.20}$$

Here we find $R_c^{TTT-iso} = 4.75$ K/s for $Pd_{40}Cu_{30}Ni_{10}P_{20}$. Note that there is some small difference in the t_n, T_n and $R_c^{TTT-iso}$ values‡ determined here from those determined in Ref. [40] due to the different values for *f* utilized in the two calculations. Further, one

† The superscript denotes that this value is obtained from isothermal TTT diagram.

‡ In Ref. [40], $t_n = 50$ s, $T_n = 680$ K, $R_c^{TTT-iso} = 2.86$ K/s.

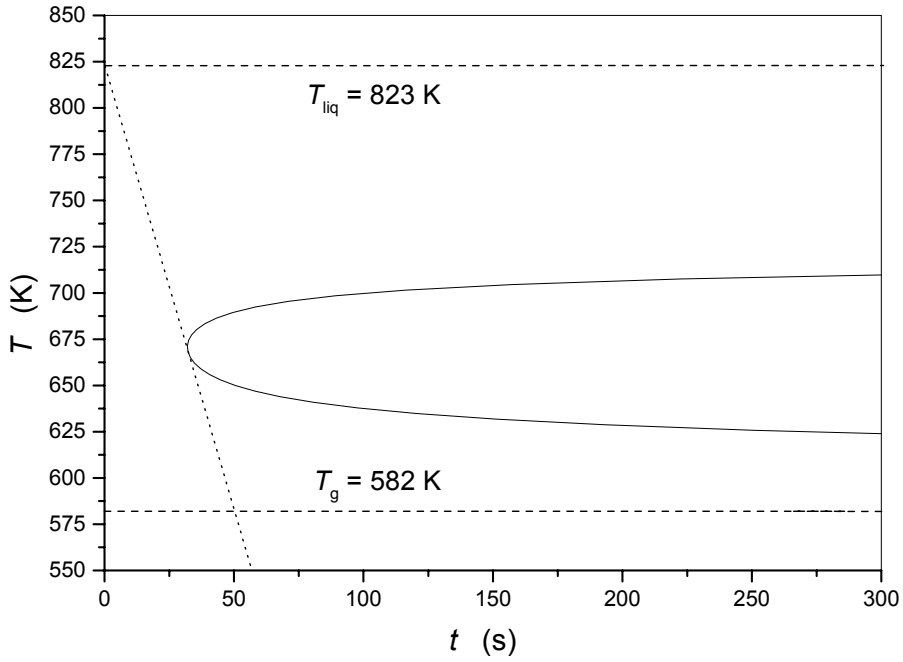

Fig 1.4 TTT (Time-Temperature-Transformation) diagram of $Pd_{40}Cu_{30}Ni_{10}P_{20}$ calculated using a crystallized volume fraction $f = 10^{-6}$. The dotted line passing through the nose of the diagram indicates the critical cooling rate required to form a glass upon cooling.

notices that the actual critical cooling rate for this alloy measured by continuous cooling experiments [40] is only ~0.33 K/s -- one order of magnitude lower than $R_c^{TTT-iso}$. This is because the calculation method used in Eq. (1.20) implicitly assumes that with a given time length, the degree of crystallization is the same in the isothermal process as in the continuous cooling. This is apparently not true since the continuous cooling process goes through a set of temperatures at which the kinetics of crystallization differs a lot. Uhlmann also realized this and made a correction by constructing continuous cooling curves following the approach of Grange and Kiefer [42]. By doing so, he found that a given degree of crystallinity (i.e., a given *f*) develops at lower temperatures and longer times during the continuous cooling than during the isothermal process, as a result of which the nose of the TTT diagram is shifted to the right (longer time) and the critical cooling rate to bypass the nose is thus lower than the one predicted by Eq. (1.20) which is solely based on isothermal TTT diagram.

Later Uhlmann and co-workers solved the continuous cooling problem directly, without the aid of isothermal TTT diagram [43]. By plugging the time dependence (equivalent to temperature dependence since $dT = -Rdt$, where R is the cooling rate assumed to be constant) of I_v and u into Eq. (1.17), one can find $f = \frac{4\pi}{3R^4}\int_{T_{liq}}^{T} I_v(T')dT'[\int_{T'}^{T} u(T'')dT'']^3$ where T_{liq} is treated as the initial temperature where the crystallization starts. Since glass formation means that the degree of crystallinity (crystallized volume fraction) developed between T_{liq} and T_g is no larger than the critical value f_c, the critical cooling rate required for glass formation can then be calculated as follows:

$$R_c = \{\frac{4\pi}{3f_c}\int_{T_{liq}}^{T_g} I_v(T')dT'[\int_{T'}^{T_g} u(T'')dT'']^3\}^{1/4} \quad (1.21)$$

The value obtained using this equation for $Pd_{40}Cu_{30}Ni_{10}P_{20}$ is 0.63 K/s ($f_c = 10^{-6}$) or 0.11 K/s ($f_c = 10^{-3}$), much closer to the measured 0.33 K/s than the $R_c^{TTT-iso}$ based on isothermal TTT diagram.

The rest of the difference between 0.63 K/s (or 0.11 K/s) and 0.33 K/s is almost negligible, considering the possible error (passed through experimental measurements of viscosity, isothermal TTT diagram measurement, and the related data fitting) in the parameters used for the calculation. Another possible source of the difference may be the approximation for the Gibbs free energy difference between the liquid and the crystal (i.e., $\Delta G = \Delta S_m(T_m - T)$). If we know the temperature dependence of the heat capacity difference between the liquid and the crystal, we can then use the full description of ΔG (i.e., Eq. (1.5)), which may bring about an even better agreement between the calculated and the measured critical cooling rates.

1.4 Frequently used criteria for the development of BMGs

Even though the classical theory of crystal nucleation and growth as demonstrated in the last section may describe well the crystallization kinetics of a glass-forming liquid and may even calculate the critical cooling rate for the glass formation to a very high precision, it is obviously not a convenient way to predict the best glass-forming compositions among a large number of candidate alloys since it requires a large amount of experimental data from each of the candidates. Therefore, ever since the first discovery

of metallic glass in 1960, continuous efforts have been devoted to the establishment of a simple and universal criterion to be used in the development of BMGs. As a result, quite a number of such criteria have been proposed to date. Although these criteria generally provide some guidance to the alloy development, there are always exceptions to every single one of them, such that excessive reliance on these criteria sometimes causes the negligence of very good metallic glass-formers. Here, however, we should still do a brief review of the most frequently used criteria. The limitations of each criterion will be discussed.

1.4.1 Reduced glass transition temperature (T_{rg})

Shortly after the discovery of the first metallic glass ($Au_{75}Si_{25}$) in 1960, Turnbull proposed that a glass tends to form easily from a liquid with a high reduced glass transition temperature (defined as $T_{rg} = \frac{T_g}{T_m}$ where T_g and T_m are the glass transition and melting temperatures, respectively [44]).

Turnbull based his argument on the assumption that a glass would form if the nucleation rate is so low that no nuclei can form virtually on the cooling time scale. He used a different form of Eq. (1.15) in Section 1.3.3 as follows:

$$I_v = \frac{k_n}{\eta} \exp[-\frac{b\alpha^3\beta}{T_r(\Delta T_r)^2}] \tag{1.22}$$

where k_n is a constant specified by the model, b is a constant determined by the nucleus shape ($b = 16\pi/3$ for a spherical nucleus), α and β are dimensionless parameters defined

as $\alpha = (NV^2)^{1/3}\sigma / \Delta H_m$ (N is the Avogadro's number, V is the molar volume, σ is the interfacial energy between the liquid and the crystal, ΔH_m is the molar heat of fusion); and $\beta = \Delta S_m / R$ (ΔS_m is the molar entropy of fusion, R is the universal gas constant). T_r and ΔT_r are the reduced temperature and reduced undercooling, respectively, defined as: $T_r = T / T_m$ and $\Delta T_r = (T_m - T)/T_m = 1 - T_r$. In the above equation, he also utilized the first order approximation for the Gibbs energy difference between the liquid and the crystal (i.e., $\Delta G = \Delta S_m (T_m - T)$). Further, he simplified the VFT expression (Eq. (1.7)) for the viscosity as:

$$\eta = 10^{-3.3} \exp\left(\frac{3.34}{T_r - T_{rg}}\right) \tag{1.23}$$

in which he equated T_g with the VFT temperature T_0 and reduced the temperatures with T_m. By substituting the values for the other parameters, namely, $k_n = 10^{35}$ Pa s/(m^3 s)[†], $b = 16\pi/3$, $\alpha\beta^{1/3} = 1/2$, he obtained the plots of $\log I_v$ vs. T_r based on different values of the reduced glass transition temperature T_{rg}. His result is reproduced here in Fig 1.5.

From these plots, Turnbull argued that the larger the T_{rg}, the smaller the magnitude of the nucleation rate and the narrower the time window available for nucleation. Further, when T_{rg} approaches 2/3 or higher, he argued, the nucleation rate is so low that within the cooling time scale in laboratory, no nuclei can form virtually (i.e., the number of nuclei

[†] Interestingly, in Turnbull's original paper [44], he assigned a wrong unit to this constant and this small mistake was followed by others for years. Here, both the magnitude and the unit have been corrected in order to reproduce his result exactly. The small mistake does not affect his conclusion, on the other hand.

formed is less than one). This argument later gained a lot of attention and became the famous '2/3 law' for glass formation from liquids.

Indeed, it has been found from practice that the easy glass-formers as a whole family usually show higher T_{rg} values than very poor glass-formers. Meanwhile, this rule can also explain the high frequency of the occurrence of BMGs around deep eutectics. In a given alloy system, the variation in T_g as the alloy composition changes is not as significant as the variation in T_l, and the low T_l around the eutectic composition thus results in a high T_{rg} $(= T_g / T_l)$[†]. However, when it comes to quantitatively comparing the glass-forming ability of two easy glass formers or pinpointing the best glass-forming composition in a certain system, there are many exceptions to this rule, including some of the BMG systems developed in this thesis, where alloys with higher T_{rg} exhibit poorer glass-forming ability.

The uncertainty in this rule comes from several factors[‡]: 1). the contributions to I_v from other parameters such as α, β, T_0 and D (the strength parameter in the VFT model of viscosity) which may also have non-negligible dependence on the alloy composition (compared to T_{rg}) have not been considered; 2). the reliability of the first order

---

[†] The replacement of T_m in Turnbull's criterion by the liquidus temperature T_l rather than the solidus temperature T_s in practice has been justified in statistical studies on a large number of BMG systems. A simple justification can be made using the fact that the primary equilibrium phase (different on different sides of an eutectic) is in most cases, the competing phase for glass formation. As such, the temperature at which this primary phase starts to form (i.e. the liquidus temperature of this phase) should be utilized for the calculation of T_{rg}.

[‡] Some of these factors were discussed in Turnbull's paper, and some were not.

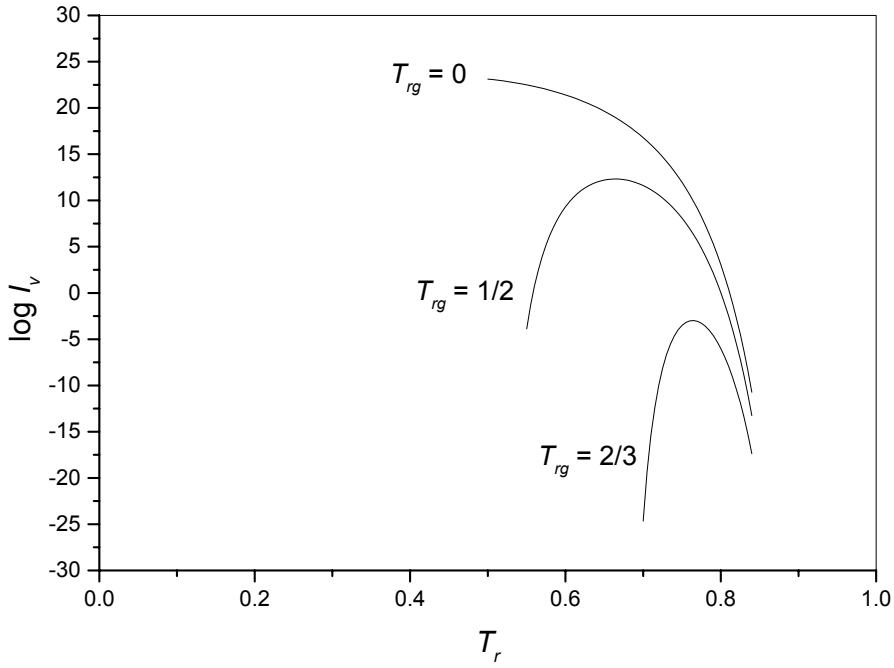

Fig 1.5 logarithm of nucleation rate (in $cm^{-3}s^{-1}$), $\log I_v$, vs. the reduced temperature, T_r, calculated at different values of the reduced glass transition temperature T_{rg} (reproduced after Ref. [44]).

approximation for ΔG used in Turnbull's analysis may not be the same good for any alloy, depending on whether or not the heat capacity difference between the undercooled liquid and the crystal states of the alloy is negligible; 3). the assumption that the glass-forming ability can be fully represented by the number of nuclei formed during cooling is not well justified (i.e., the contribution from crystal growth to crystallization has not been clarified in this rule).

1.4.2 Multi-component rule (confusion principle)

The sudden improvement in the glass-forming ability from the early poor metallic glass formers (before the end of the 1980's) to the first bulk metallic glasses (Zr-, La-, and Mg-based, found at the end of the 1980's and the beginning of the 1990's), and the historical fact that the former were mostly binary alloys while the latter were invariantly multi-component alloys have led to an impression that good glass-forming ability solely belongs to multi-component systems. For a very long time, it has been considered a 'must' rule for BMG formation that the system contain at least three elements [45]. Further, a 'confusion principle' has been proposed for developing new BMGs which states that 'the more elements involved, the lower the chance that the alloy can select viable crystal structures, and the greater the chance of glass formation' [46].

While these rules make a certain amount of sense about the chemical complexity required by BMG formation, their importance can't be over-exaggerated, considering their purely empirical nature. The effect of increased chemical complexity on the glass-forming ability may well be twofold. On one hand, it may cause denser packing in the liquid and lead to higher viscosity and lower atomic mobility; on the other hand, it may introduce

new competing crystalline phases with lower energy as well. Simple evidence for this is that the addition of more randomly selected elements -- or even those selected with caution (following other empirical rules such as those discussed below) -- to the two known easiest metallic glass formers, namely $Pd_{40}Cu_{30}Ni_{10}P_{20}$ and $Zr_{41.2}Ti_{13.8}Cu_{12.5}Ni_{10}Be_{22.5}$, actually has a higher chance of ruining the superior glass-forming ability of these alloys[†].

As a matter of fact, with more and more BMG alloy compositions being reported, it seems quite likely that the ideal number of components for most good metallic glass formers sits between three and five, with few exceptions on either side of this range.

Moreover, it will be shown in Chapter 3 that BMG formation is not solely a privilege of multi-component alloys. Instead, it may appear in as simple as binary systems with only two components.

1.4.3 Atomic size mismatch

There are basically two different expressions for the requirements on atomic size difference by BMG formation. One expression states that BMG formation requires, or at least prefers, significantly different atomic sizes among main constituents [45]. The main consideration underlying this expression is that a large difference in atomic sizes helps destabilize the competing crystalline phase(s) by producing large lattice stress and thus increasing the energy of the crystalline state [47]. This seems reasonable considering the Hume-Rothery rule in classical metallurgy which states that the larger the atomic size

[†] This has been manifested directly by the fact that no easier metallic glass formers based on these two, but comprised of more components, have been discovered.

difference between solute and solvent elements, the smaller the solid solubility [48]. In order to form a glass stable crystalline solid solutions have to be destabilized. A quantitative model was established based on this consideration [47], which led to a satisfying correlation between the hence calculated and the experimentally observed minimum solute concentration in a large number of binary glass-forming alloys. However, this atomic level stress model does not provide specific information about the optimal solute concentration corresponding to the highest glass-forming ability in a given system, especially a multi-component system.

The other expression of the atomic size criterion for BMG formation is based on the topology of local atomic packing in the liquid state [49-51]. By analyzing the packing geometry within the first coordinate shell around a solute atom, Miracle first found that certain values of the atomic size ratio of the solute atom to the solvent atom can lead to the maximum, 1, in the local packing efficiency[†] [49]. A survey on the reported metallic glasses supported the idea that these values are preferred by metallic glass formation. Later [51], Miracle extended his model by building a unit lattice cell in which the single-shell clusters (each has a layer of solvent atoms on the surface of a single solute atom) occupy the vertices. He then applied his model to multi-component BMGs by introducing a second and a third topological species to occupy the octahedral and the tetrahedral interstices within the cluster lattice. He even suggested a quantitative way to calculate the concentrations of each topological species of components. A reasonable agreement between the hence calculated and the experimentally obtained optimal compositions of

[†] The maximum local packing efficiency, 1, corresponds to a case in which the solvent atoms (surrounding and touching a given solute atom) tightly touch each other with no spacing between two neighboring solvent atoms.

many BMG alloys was demonstrated in his paper. Nevertheless, his model still has limitations: 1). it has been based solely on the topology of local atomic packing within a glass (or its liquid) without considering other factors such as the chemical interactions among the constituent species; 2). the mechanism of how the topological factor contributes to the thermodynamics, kinetics and the glass-forming ability of glass-forming liquids is not clarified, or at least not quantified; 3). it provides no information about the long range atomic packing which may actually be even more important than the local packing to the kinetics of undercooled liquids, considering the free volume model of viscosity. As a matter of fact, quite a number of the recently discovered BMGs, including some developed in this thesis work, can't be fully explained by this model in terms of composition.

1.4.4 Chemical interactions among constituent elements

According to thermodynamics, the free energy change caused by mixing two different species (*A* and *B*) is expressed as:

$$\Delta G_{mix} = \Omega X_A X_B + RT(X_A \ln X_A + X_B \ln X_B) \tag{1.24}$$

where X_A and X_B are the atomic concentrations, and Ω is proportional to the molar heat of mixing (chemical interaction) between these two species[†]. Therefore, for a given X_A and X_B, a negative heat of mixing (an attractive interaction) tends to lower the system's energy. If this mixing effect is more influential in the liquid (undercooled) state than in the crystalline state, then the Gibbs free energy difference between these two states (i.e.,

[†] The proportional coefficient is the coordination number which may differ from the liquid to crystal state.

the driving force for crystallization) can be lowered, and thus, the chance of glass formation will be enhanced. This consideration has been proposed as another empirical rule for BMG development [45] since many of the reported BMG systems appear to have relatively large negative heat of mixing. However, the assumption made above (i.e., the different effects of mixing on the liquid and the crystalline states) may not be well satisfied in certain cases. As a result, excessive reliance on this empirical rule may not be advisable.

1.4.5 Considerations based on phase diagrams

Phase diagrams are handy tools for BMG development because they provide important information about both the liquid and the competing crystalline phases. Moreover, many other empirical criteria such as the ones introduced in the previous sections are often more or less reflected by phase diagrams.

Since high glass-forming ability usually appears around deep eutectics, it is often a good choice to start with an alloy system whose phase diagram contains deep eutectics. Zr-Be (Fig 1.6) is a good example of such systems. One can notice that there is a dramatic decrease (of ~890 K) in the liquid temperature when 35% Be is added to pure Zr to form the binary eutectic. This particular system has also another attractive feature: the eutectic zone is far from both stable intermetallic compounds and terminal solid solution (Be in Zr), which indicates that in order for the liquid (around the eutectic zone) to crystallize, the local chemical composition inside the liquid has to undergo a severe change by significant atomic rearrangement.

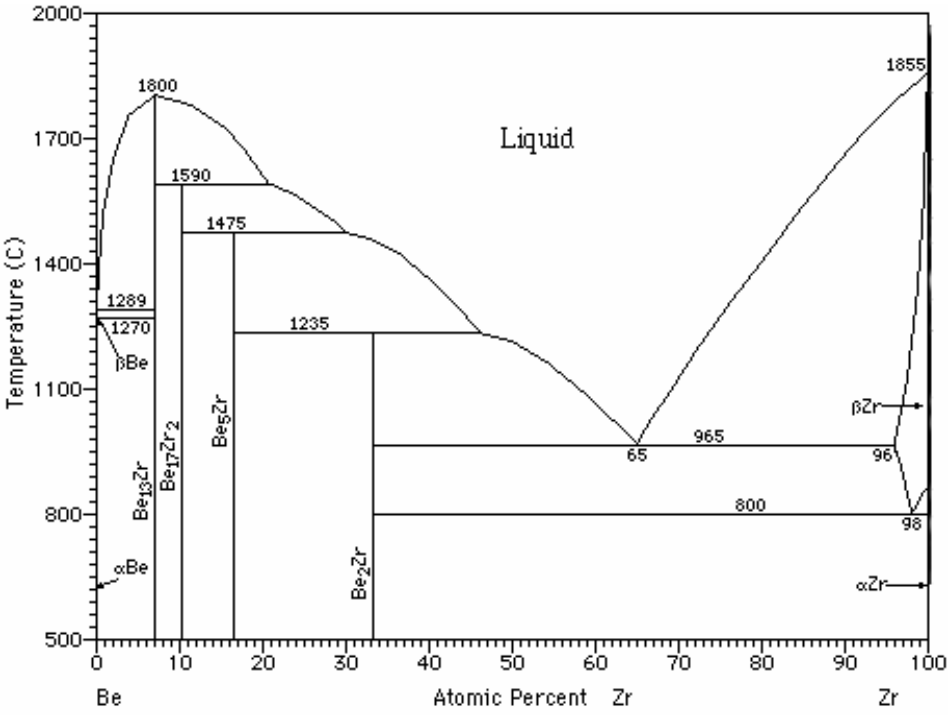

Fig 1.6 Binary phase diagram of Zr-Be system (reproduced from Ref. [52])

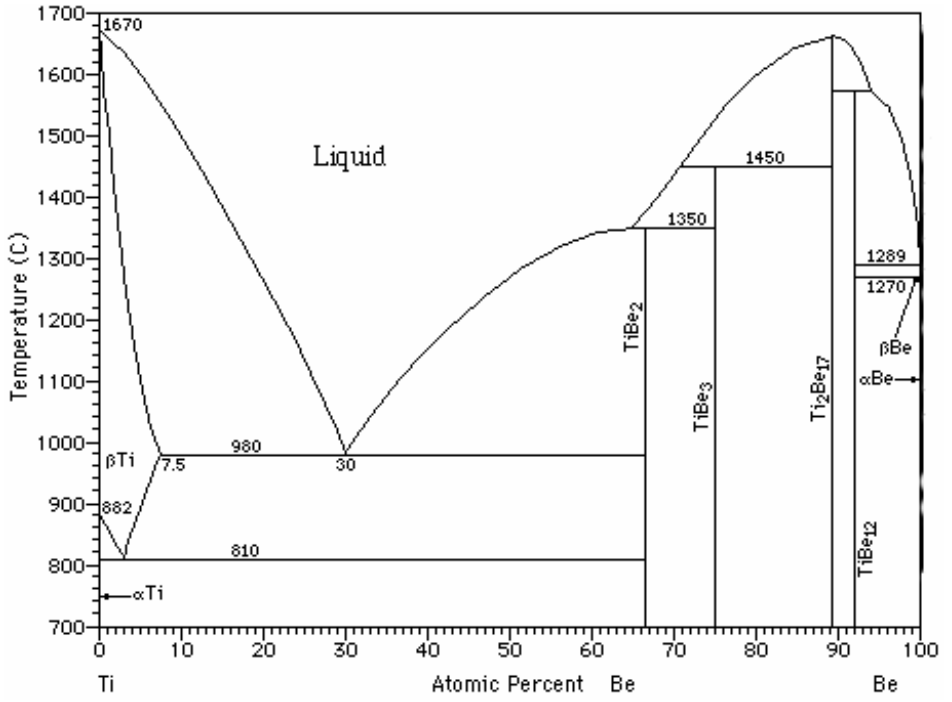

Fig 1.7 Binary phase diagram of Ti-Be system (reproduced from Ref. [52])

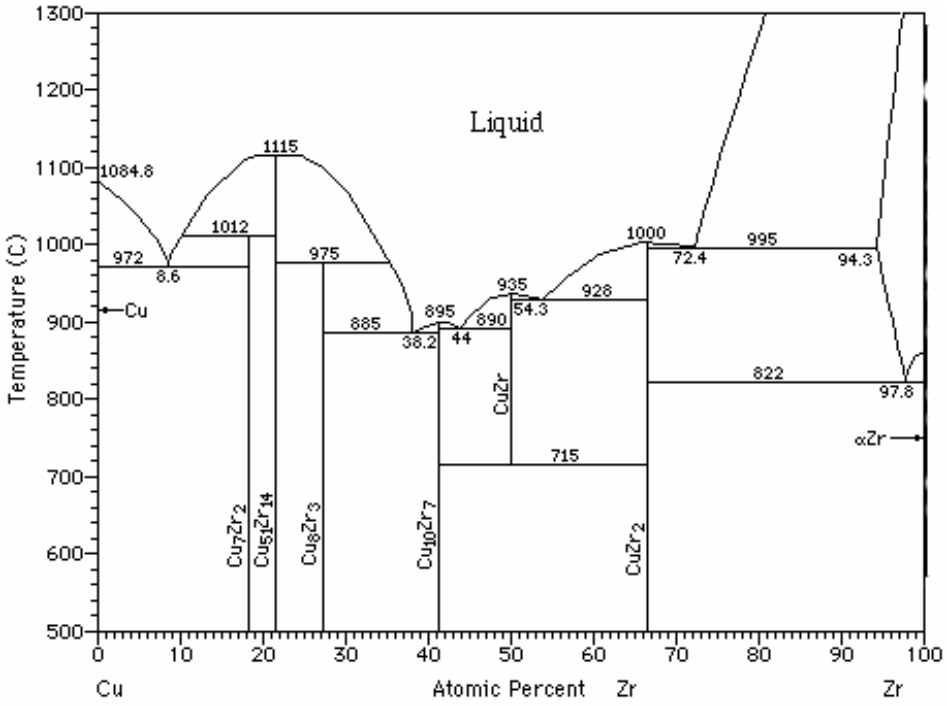

Fig 1.8 Binary phase diagram of Zr-Cu system (reproduced from Ref. [52])

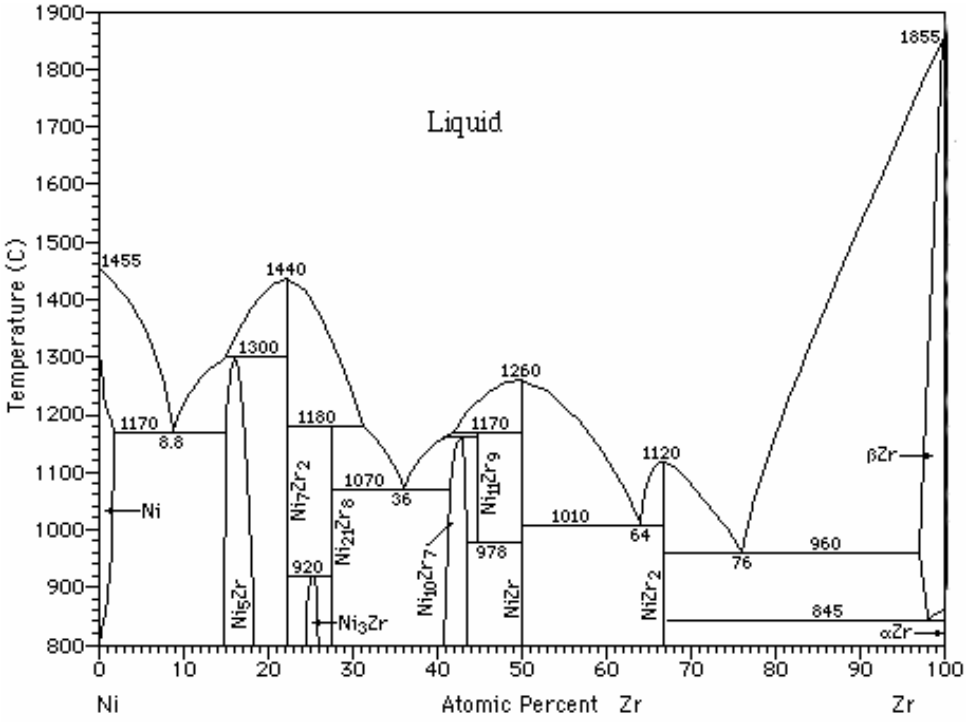

Fig 1.9 Binary phase diagram of Zr-Ni system (reproduced from Ref. [52])

In order to further improve glass-forming ability, additional alloying elements can be introduced to the starting system. Many studies have shown that the combination of several simple eutectic systems often leads to an even deeper eutectic in the resulting complex system. For example, both Zr-Be (Fig 1.6) and Ti-Be (Fig 1.7) binary phase diagrams exhibit a deep eutectic on the Zr-rich side, and replacing part of Zr in Zr-Be alloys (around its binary eutectic composition) with certain amount of Ti further lowers the liquidus temperature and brings the alloys closer to an even deeper ternary eutectic. Fig 1.8 and 1.9 show the binary phase diagrams of Zr-Cu and Zr-Ni systems, respectively. One notices two important features on the Zr-rich side (Zr content > 50%) of both of these two diagrams: 1). there exist a couple of deep binary eutectics; and 2). the competing crystalline phases are the intermetallic compounds ZrM and Zr_2M (where M=Cu or Ni) [†] which do not have counterparts in Zr-Be system. Therefore, one expects that by introducing Ni and/or Cu into Zr(Ti)-Be system, the eutectic temperature will be further lowered and, meanwhile, the crystallization of the liquid will become more difficult due to the increase in the number of competing crystalline phases with different structures[‡].

When adding more alloying elements to a base system, it is important to avoid introducing very stable crystals. For example, when adding B into Zr-based alloys, the amount of B has to be carefully controlled because otherwise a very stable compound (ZrB_2, as shown in Fig 1.10) may be encountered.

[†] A closer look at the database for the compounds discloses that the structures of these compounds are even different for Cu and for Ni, although their chemical formulae are the same [52].

[‡] Also noteworthy is that none of the newly introduced competing phases (i.e., ZrM and Zr_2M, where M=Cu or Ni) is much more stable than the original competing phases (i.e., $ZrBe_2$ and Be-in-Zr solid solution), judging from the melting temperatures of all these crystals.

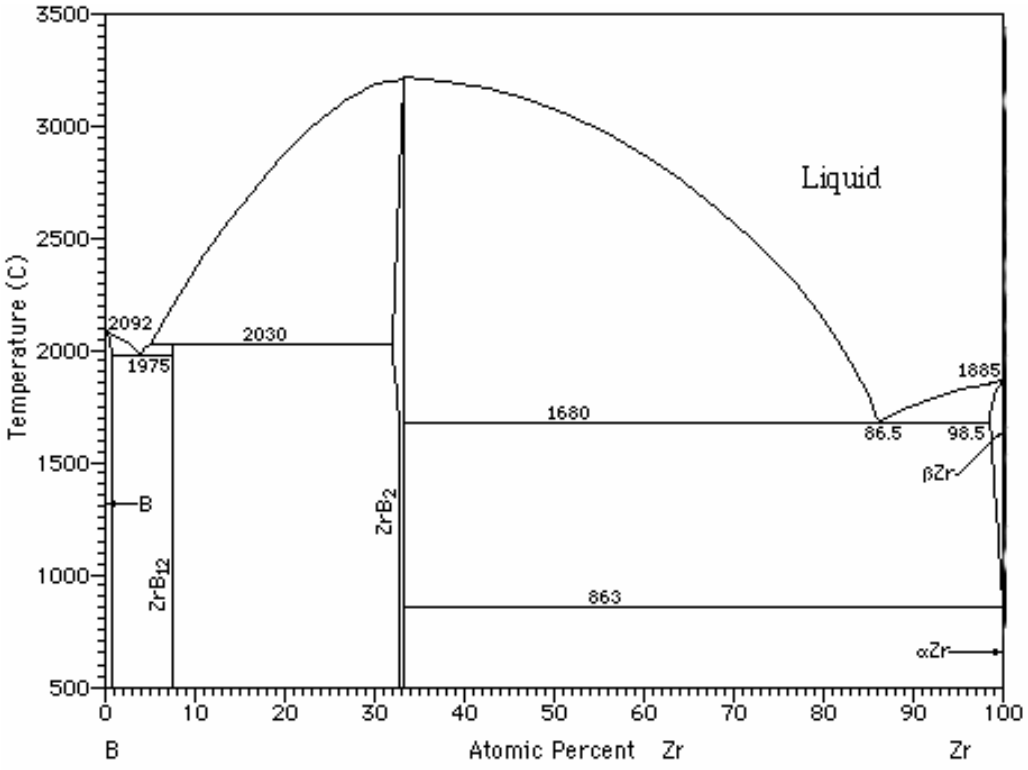

Fig 1.10 Binary phase diagram of Zr-B system (reproduced from Ref. [52])

Like other empirical criteria, the application of phase diagrams in BMG development also has limitations. On one hand, most of the available phase diagrams refer to only thermodynamically stable phases and provide no information about metastable or even unstable phases that may come up in rapid cooling of a liquid. On the other hand, the phase diagrams for complex alloy systems are generally not available and have to be conjectured from the phase diagrams of the sub-systems. The conjecture may not be very reliable sometimes, especially when unknown crystalline phases are resulted from the combination of sub-systems.

References

[1] M. H. Cohen and D. Turnbull, Nature **203**, 964 (1964).

[2] C. A. Angell, Science **267**, 1924 (1995).

[3] T. A. Waniuk, J. Schroers and W. L. Johnson, Appl. Phys. Lett. **78**, 1213 (2001).

[4] L. E. Tanner and R. Ray, Acta Metall. **27**, 1727 (1979).

[5] A. L. Greer, Science **267**, 1947 (1995).

[6] N. Nishiyama and A. Inoue, Mater. Trans. JIM **38**, 464 (1997).

[7] H. Choi-Yim, D. H. Xu and W. L. Johnson, Appl. Phys. Lett. **82**, 1030 (2003).

[8] D. H. Xu, B. Lohwongwatana, G. Duan, W. L. Johnson and C. Garland, Acta Mater. **52**, 2621 (2004).

[9] D. H. Xu, G. Duan and W. L. Johnson, Phys. Rev. Lett. **92**, 245504 (2004).

[10] D. H. Xu, G. Duan, W. L. Johnson and C. Garland, Acta Mater. **52**, 3493 (2004).

[11] W. Klement, R. H. Willens and P. Duwez, Nature **187**, 869 (1960).

[12] W. Buckel, Z. Phys. **138**, 136 (1954).

[13] R. Ray, B. C. Giessen and N. J. Grant, Scr. Metall. **2**, 357 (1968).

[14] R. C. Ruhl, B. C. Giessen, M. Cohen and N. J. Grant, Acta Metall. **15**, 1693 (1967).

[15] M. Mehra, A. Williams and W. L. Johnson, Phys. Rev. B **28**, 624 (1983).

[16] A. Calka, M. Madhava, D. E. Polk and B. C. Giessen, Scr. Metall. **11**, 65 (1977).

[17] P. Duwez and S. C. H. Lin, J. Appl. Phys. **38**, 4096 (1967).

[18] T. Masumoto and R. Maddin, Acta Metall. **19**, 725 (1971).

[19] A. J. Drehman and A. L. Greer, Acta Metall. **32**, 323 (1984).

[20] A. Peker and W. L. Johnson, Appl. Phys. Lett. **63**, 2342 (1993).

[21] A. Inoue, K. Kita, T. Zhang and T. Masumoto, Mater. Trans. JIM **30**, 722 (1989).

[22] X. Wang, I. Yoshii, A. Inoue, Y. H. Kim and I. B. Kim, Mater. Trans. JIM **40**, 1130 (1999).

[23] S. Yi, T. G. Park and D. H. Kim, J. Mater. Res. **15**, 2425 (2000).

[24] S. Yi, J. S. Jang, W. T. Kim, D. H. Kim, Mater. Lett. **48**, 258 (2001).

[25] X.H. Lin, and W.L. Johnson, J. Appl. Phys., **78**, 6514 (1995).

[26] W. Kauzmann, Chem. Rev. **43**, 219 (1948).

[27] R. Busch, Y. J. Kim and W. L. Johnson, J. Appl. Phys. **77**, 4039 (1995).

[28] R. Busch, Y. J. Kim, W. L. Johnson, A. J. Rulison, W. K. Rhim and D. Isheim, Appl. Phys. Lett. **66**, 3111 (1995).

[29] A. Masuhr, T. A. Waniuk, R. Busch and W. L. Johnson, Phys. Rev. Lett. **82**, 2290 (1999).

[30] H. Vogel, Z. Phys. **22**, 645 (1921).

[31] G. S. Fulcher, J. Am. Ceram. Soc. **8**, 339 (1925).

[32] G. Tammann and W. Z. Hesse, Anorg. Allgem. Chem. **156**, 245 (1926).

[33] G. S. Grest and M. H. Cohen, Adv. Chem. Phys. **48**, 455 (1981).

[34] R. Bohmer, K. L. Ngai, C. A. Angell and D. J. Plazek, J. Chem. Phys. **99**, 4201 (1993).

[35] D. N. Perera, J. Phys.: Condens. Matter **11**, 3807 (1999).

[36] P. C. Si, X. F. Bian, J. Y. Zhang, H. Li, M. H. Sun and Y. Zhao, J. Phys.: Condens. Matter **15**, 5409 (2003).

[37] N. Nishiyama and A. Inoue, Acta Mater. **47**, 1487 (1999).

[38] D. M. Herlach, Mater. Sci. Eng. R **12**, 177 (1994).

[39] I. R. Lu, G. Wilde, G. P. Gorler and R. Willnecker, J. Non-Cryst. Solids **250-252**, 577 (1999).

[40] J. F. Loffler, J. Schroers and W. L. Johnson, Appl. Phys. Lett. **77**, 681 (2000).

[41] D. R. Uhlmann, J. Non-Cryst. Solids **7**, 337 (1972).

[42] R. A. Grange and J. M. Kiefer, Trans. ASM **29**, 85 (1941).

[43] M. C. Weinberg, D. R. Uhlmann and E. D. Zanotto, J. Am. Ceram. Soc. **72**, 2054 (1989).

[44] D. Turnbull, Contemp. Phys. **10**, 473 (1969).

[45] A. Inoue and A. Takeuchi, Mater. Trans. **43**, 1892 (2002).

[46] A. L. Greer, Nature **366**, 303 (1993).

[47] T. Egami and Y. Waseda, J. Non-cryst. Solids **64**, 113 (1984).

[48] W. Hume-Rothery, R. E. Smallman and C. W. Haworth, The Structure of Metals and Alloys, 5th Ed. (The Institute of Metals, London, 1969).

[49] D. B. Miracle, W. S. Sanders and O. N. Senkov, Philos. Mag. **83**, 2409 (2003).

[50] D. B. Miracle, O. N. Senkov, W. S. Sanders and K. L. Kendig, Mat. Sci. Eng. A. **375-77**, 150 (2004).

[51] D. B. Miracle, Nature Mater. 3, 697 (2004).

[52] *Binary Alloy Phase Diagrams*, 2nd ed., T. B. Massalski, ed. (ASM International, Metals Park, OH, 1990).

Chapter 2

Formation and properties of Ni-based BMGs in Ni-Cu-Ti-Zr-Al system

2.1 Introduction

Although the early discovered BMGs such as Zr- [1,2], La- [3,4], Mg- [5] based alloys provided for the first time an excellent combination of high glass-forming ability and good mechanical properties, they still have certain limitations as candidates for structural materials. For example, their glass transition temperatures are usually quite low, which prevents them from high temperature applications; their relatively high material costs and low elastic modulus also leave room for further improvement. Accordingly, there is a growing interest in identifying processable amorphous alloys with greater strength, elastic modulus, hardness, and lower material costs. Of particular interest are the alloys based on common metals like Fe, Co, Ni, etc.

As to Ni-based alloys, although quite a few glass-forming systems with very high strength (typically larger than 2 GPa, and some even approaching 3 GPa) have been reported, the glass-forming abilities achieved so far are very limited. For example, Ni-Nb-Cr-Mo-P-B alloys could only form 1 mm diameter amorphous rods [6]. The more recent Ni-Ti-Zr-(Si,Sn) [7], Ni-Nb-Ti-Zr-Co-Cu [8] and Ni-Nb-Sn (co-developed by H. Choi-Yim and the author at Caltech) [9] alloys could be cast to 2 mm diameter glassy rods, but no larger. Further, some of these reported systems [6,7] comprise metalloids in their chemical compositions which limit their manufacturability. For broader engineering

applications or scientific studies on Ni-based glasses, it is necessary to develop new Ni-based alloys with higher glass-forming abilities and better manufacturability.

This chapter reports on the formation, thermal and mechanical properties of a new family of Ni-based bulk glass-forming alloys with the formula $Ni_xCu_{a-x}Ti_yZr_{b-y}Al_{10}$ (a~b~45, in at.%) which possess a critical casting thickness ranging from 2mm up to 5mm[†].

2.2 Experimentals

The ingots of the alloys studied in this work were prepared by arc melting mixtures of ultrasonically-cleansed elemental metals having a purity of 99.5 at.% or higher. The arc melting was performed in a Ti-gettered high purity Argon atmosphere. Each ingot was re-melted in the arc melter at least three times aimed at obtaining chemical homogeneity. The alloyed ingots were then re-melted under high vacuum in a quartz tube using an induction-heating coil, and then injected through a small nozzle into a copper mold using high purity argon at a pressure of 1-2 atm. The copper molds have internal rectangular cavities with various thicknesses ranging from 0.5 mm to 5 mm. For comparison purposes, very thin samples of thickness ~60 μm were also prepared using an Edmund Buhler D-7400 splat quencher. Both the thin samples and the transverse cross sections of the bulk cast samples (cut along a plane normal to the length of the samples) were examined by X-ray diffraction (XRD), using a 120° position sensitive detector (Inel) and a collimated Co Kα source. The amorphous structures of the bulk cast samples were further confirmed by transmission electron microscopy (TEM) analyses performed on their cross sections. The glass transition and crystallization behaviors of all samples were

[†] These results have been published in Ref. [10]. A patent has been applied for these new Ni-based BMGs.

examined with a differential scanning calorimeter (Perkin-Elmer DSC 7) at a heating rate of 0.33 K/s. Vicker's hardness was measured on fully amorphous rectangular cast strips using a Leitz micro-hardness tester. Young's modulus, shear modulus and Poisson ratio were obtained by measuring the longitudinal and shear sound velocities in the fully amorphous strips with an ultrasonic device and substituting the velocities into a set of formulas to be shown in Section 2.3.5. 2 mm (diameter) x 4 mm (height) cylindrical cast samples were used to measure compressive mechanical properties of the alloys on an Instron testing machine at a strain rate of ~$4x10^{-4}$ s^{-1}. Prior to the compression test, both the top and the bottom of each specimen were examined with X-ray to make sure the casting was successful and that no crystallization due to unexpected factors occurred.

2.3 Results and discussions

2.3.1 Ternary $Ni_{45}Ti_{20}Zr_{35}$ alloy

Table 2.1 lists some examples of the newly discovered bulk metallic glasses in an order that reflects the sequential optimization of successive alloy additions which resulted in the improvement of the critical casting thickness for obtaining fully glassy samples.

The first phase of this work was the discovery of the ternary thin glass former, $Ni_{45}Ti_{20}Zr_{35}$, which produced a 0.5 mm thick partially amorphous strip using injection mold casting. The XRD and DSC scans of this ternary alloy are included in Fig 2.1 and Fig 2.2, respectively. Although there is some evidence of crystallinity on the XRD pattern in Fig 2.1, the apparent diffuse background represents a large fraction of amorphous phase in the sample. This is further confirmed by the DSC scan in Fig 2.2 which gives a

total exothermic heat release of 52 J/g caused by the crystallization of the amorphous fraction of the specimen. The T_g and T_{x1} (marked in the figure by arrows) of this alloy are 725 K and 752 K, respectively, and thus, the stable undercooled liquid range is $\Delta T=T_{x1}-T_g=27$ K.

Table 2.1 Examples of the new Ni-based amorphous alloys developed in this work (T_g and T_{x1} were measured with DSC at a heating rate of 0.33K/s)

Alloy Composition (at.%)	Critical Casting thickness (mm)	T_g (K)	T_{x1} (K)	$\Delta T=T_{x1}-T_g$ (K)
$Ni_{45}Ti_{20}Zr_{35}$	~0.5	725	752	27
$Ni_{45}Ti_{20}Zr_{27}Al_8$	<0.5	761	802	41
$Ni_{45}Ti_{20}Zr_{25}Al_{10}$	2	773	818	45
$Ni_{45}Ti_{20}Zr_{23}Al_{12}$	<0.5	783	832	49
$Ni_{40}Cu_6Ti_{16}Zr_{28}Al_{10}$	3	765	807	42
$Ni_{40}Cu_5Ti_{17}Zr_{28}Al_{10}$	4	762	808	46
$Ni_{40}Cu_5Ti_{16.5}Zr_{28.5}Al_{10}$	5	763	809	46
$Ni_{39.8}Cu_{5.97}Ti_{15.92}Zr_{27.86}Al_{9.95}Si_{0.5}$	5	768	815	47

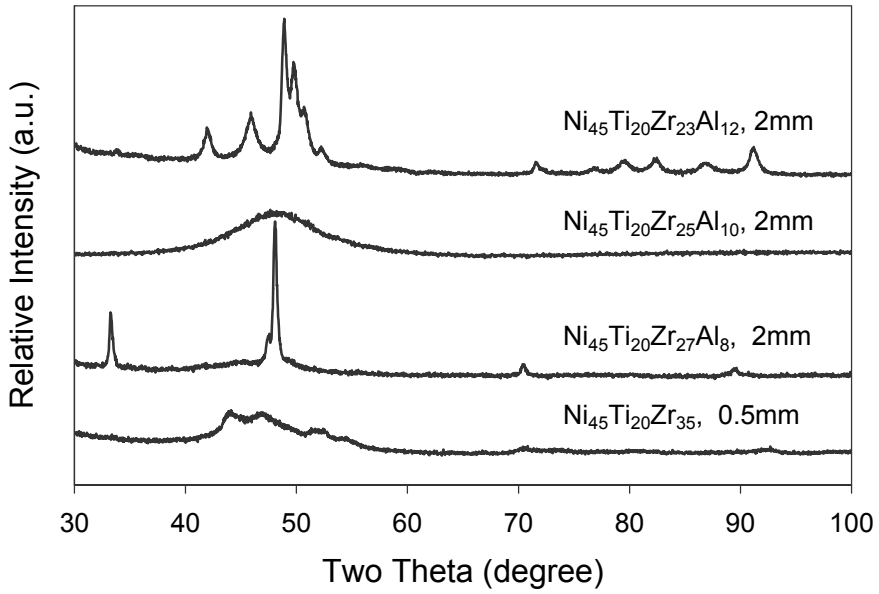

Fig 2.1 XRD patterns of selected ternary and quaternary alloys taken with a Co Kα source.

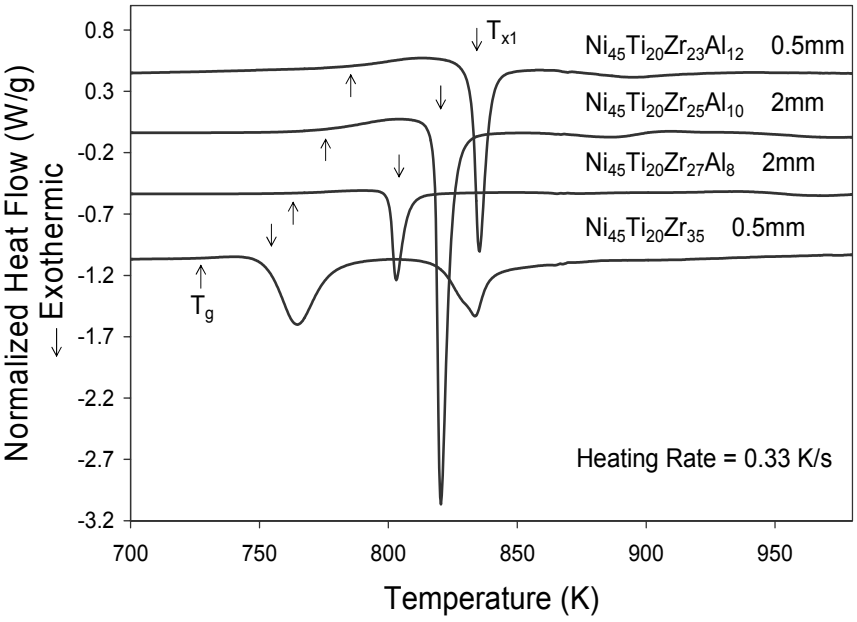

Fig 2.2 DSC scans of selected ternary and quaternary alloys at a heating rate of 0.33 K/s.

2.3.2 Quaternary $Ni_{45}Ti_{20}Zr_{35-x}Al_x$ alloys

Fig 2.1 shows the structural effects of subsequent Al additions to the ternary alloy (in replacement of Zr). In Fig 2.1, the quaternary samples used for taking XRD patterns are all 2 mm-thick strips and the patterns were taken from the transverse cross sections of the strips. The sample with 8% Al shows a weak broad background together with some nanocrystalline-like peaks, indicating a two-phase (amorphous phase + crystalline phase) partially crystallized structure. The sample with 10% Al only shows a series of broad diffraction maxima without any observable crystalline Bragg peaks, indicating a fully amorphous structure. The sample with 12% Al shows many crystalline peaks without any noticeable diffuse background, indicating the formation of one or more complex intermetallic compounds. Clearly, the alloy with 10% Al is the best glass former in this quaternary alloy series.

Fig 2.2 presents the thermodynamic effects of the Al additions. As can be seen from these DSC scans, as well as from Table I, the T_g, T_{x1}, and ΔT all increase monotonically as the Al content increases from 8% to 10% and 12%. It was previously proposed [11] that the glass-forming ability increases with ΔT or, in other words, alloys with higher ΔT values tend to have higher glass-forming abilities. However, the diffraction results in Fig 2.1 clearly show that the highest glass-forming ability in the current quaternary alloy series occurs at 10% Al which does not correspond to the highest ΔT value. The alloy with the highest ΔT value (i.e., $Ni_{45}Ti_{20}Zr_{23}Al_{12}$) seems to have the lowest glass forming ability among the three alloys, judging from diffraction patterns in Fig 2.1. A similar discrepancy between glass forming ability and thermal stability (i.e., ΔT) has been

observed in other alloy systems [12-14]. For the Vitreloy series of BMGs [12], a decomposition mechanism was used to explain why the best glass former does not have the highest thermal stability upon heating at a constant rate. Further work including SANS (Small Angel Neutron Scattering) experiments is needed to clarify if the same mechanism is involved in the current alloys.

2.3.3 Quinary $Ni_xCu_{a-x}Ti_yZr_{b-y}Al_{10}$ alloys (a~b~45)

Fig 2.3, 2.4, and 2.5 present further major improvements achieved by adding copper to the above quaternary alloy $Ni_{45}Ti_{20}Zr_{25}Al_{10}$. With small amounts of copper and small adjustments in compositions, thicker, fully amorphous samples have been successfully prepared. Without Cu, the quaternary alloy is significantly crystallized at 3 mm thickness as shown in Fig 2.3. The appropriate additions of Cu prevent the formation of the intermetallic compounds yielding fully amorphous samples. The best glass forming ability was achieved from $Ni_{40}Cu_5Ti_{16.5}Zr_{28.5}Al_{10}$ ('RAG2', in the following) which has a critical casting thickness above 5 mm. To the best of our knowledge, this is the highest critical casting thickness ever obtained for Ni-based BMGs. To confirm the fully amorphous structure of the 5mm thick strip of RAG2, TEM analysis was also performed on its transverse cross section. From Fig 2.4, one can see its electron diffraction pattern only comprises a series of diffuse halo rings. No distinct evidence of sharp crystalline

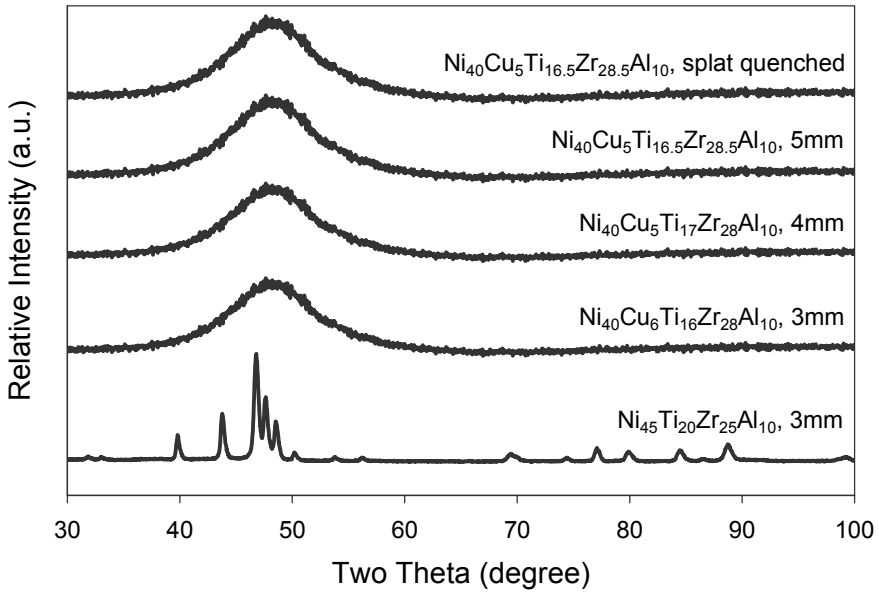

Fig 2.3 XRD patterns of selected quaternary and quinary alloys taken with a Co Kα source

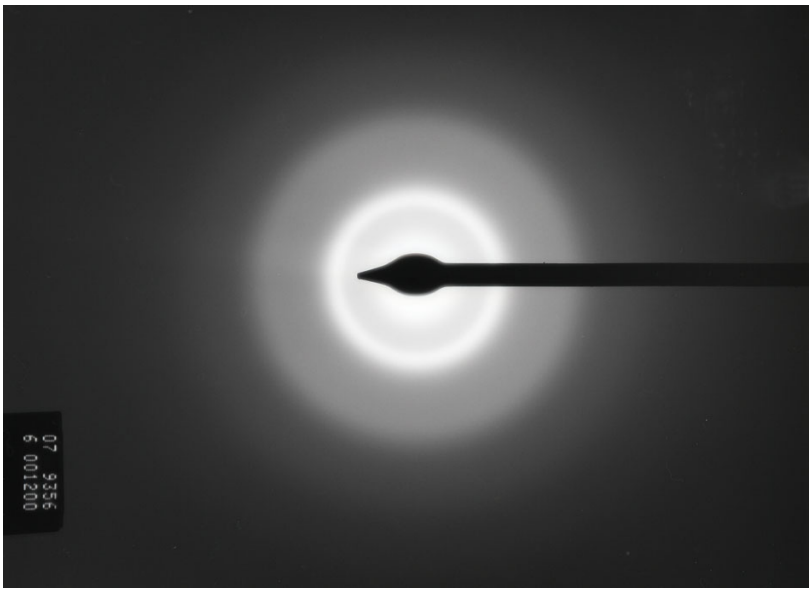

Fig 2.4 Electron diffraction pattern taken from the transverse cross section of a 5mm thick $Ni_{40}Cu_5Ti_{16.5}Zr_{28.5}Al_{10}$ strip

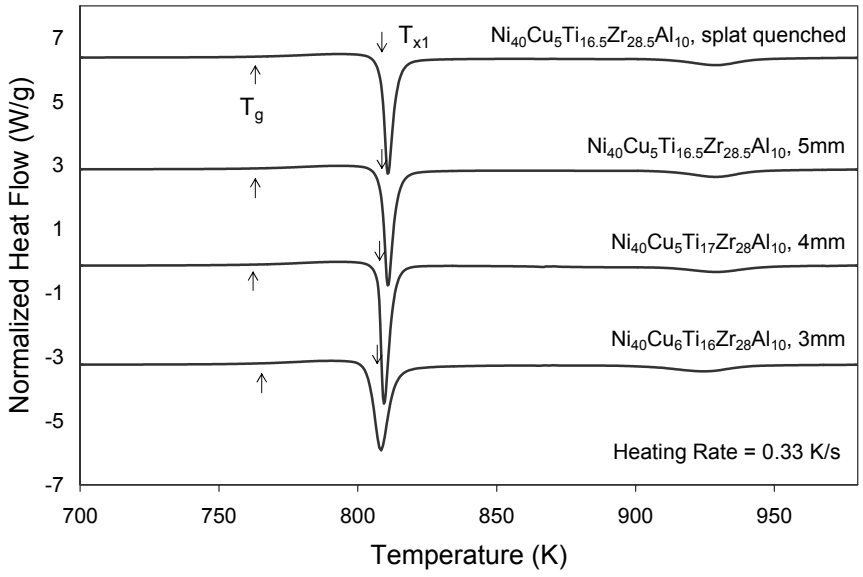

Fig 2.5 DSC scans of selected quaternary and quinary alloys at a heating rate of 0.33 K/s

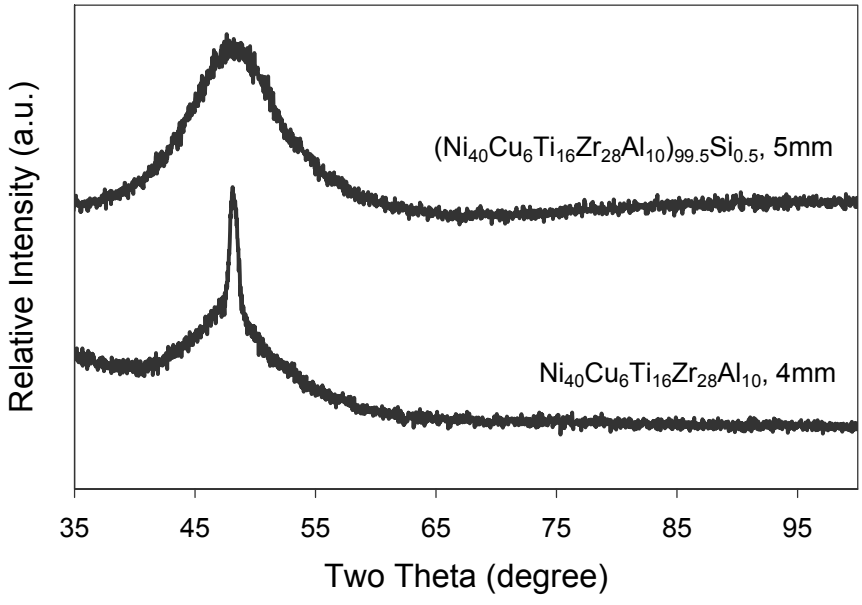

Fig 2.6 The effect of small amount Si addition

rings was found anywhere across the specimen. Therefore, it is clear that the 5 mm strip of RAG2 indeed has a fully amorphous structure. TEM analyses were also performed on other bulk samples. The results, which are not shown here, are all in good agreement with the XRD analyses.

Fig 2.5 shows the DSC traces of the quinary alloys. All these samples exhibit an endothermic glass transition and a fairly wide undercooled liquid region, followed by one or more exothermic events characteristic of crystallization. Their T_g, T_{x1}, and ΔT values are listed in Table 2.1. For a comparison, a DSC trace taken from a ~60 μm thick splat quenched sample of RAG2 is also included in Fig 2.5. Within the measurement range, there is no appreciable difference in the T_g, T_{x1} and ΔH_x (total enthalpy of crystallization) values of the splat quenched sample and the 5mm thick strip of RAG2. This again confirms the fully amorphous structure of the bulk cast sample.

2.3.4 Effect of small Si additions

A small amount Si addition also appears to provide an improvement as illustrated in Fig 2.6. Without Si, 4 mm thick $Ni_{40}Cu_6Ti_{16}Zr_{28}Al_{10}$ strip shows an observable Bragg peak superimposed on the broad, amorphous diffraction band, indicating that small nanocrystals have precipitated from the amorphous matrix. However, with 0.5% Si, the alloy $(Ni_{40}Cu_6Ti_{16}Zr_{28}Al_{10})_{99.5}Si_{0.5}$ is fully amorphous up to 5 mm, as shown by the absence of any sharp crystalline peaks on the XRD pattern in Fig 2.6. The thermal parameters of this Si-containing alloy are also included in Table 2.1, where it can be seen that the small Si addition enlarges the undercooled liquid region ΔT by increasing the crystallization temperature (T_{x1}) while leaving T_g almost unchanged. This enhancement

of glass forming ability and stability of the glassy state by adding small amounts of Si agrees with previous reports for Zr-based BMG's [16].

2.3.5 Mechanical tests

Vicker's hardness and elastic modulii were measured using those cast strips confirmed to be fully amorphous by both XRD and DSC. Selected results are shown in Table 2.2. The modulii and Poisson ratio were obtained by measuring the sound propagation velocities of plane waves (longitudinal and transverse, C_l and C_s, respectively) in the alloys, then using the following relations (valid for isotropic materials such as glasses):

$\nu=(2-x)/(2-2x)$=Poisson ratio, where $x=(C_l/C_s)^2$

$G=\rho*C_s^2$ = shear modulus, where ρ is density

$E=G*2(1+\nu)$ = Young's modulus.

Table 2.2 Some measured mechanical properties of selected alloys

Alloy Composition (at.%)	Vicker's Hardness (Kg/mm^2)	Poisson Ratio	Shear Modulus (GPa)	Young's Modulus (GPa)	Fracture Strength (GPa)
$Ni_{45}Ti_{20}Zr_{25}Al_{10}$	791	0.36	42	114	2.37
$Ni_{40}Cu_6Ti_{16}Zr_{28}Al_{10}$	780	0.361	40.9	111	2.18
$Ni_{40}Cu_5Ti_{17}Zr_{28}Al_{10}$	862	0.348	49.7	133.9	2.3
$Ni_{40}Cu_5Ti_{16.5}Zr_{28.5}Al_{10}$	800	0.355	45.2	122	2.3
$Ni_{39.8}Cu_{5.97}Ti_{15.92}Zr_{27.86}Al_{9.95}Si_{0.5}$	829	0.36	43	117	2.32

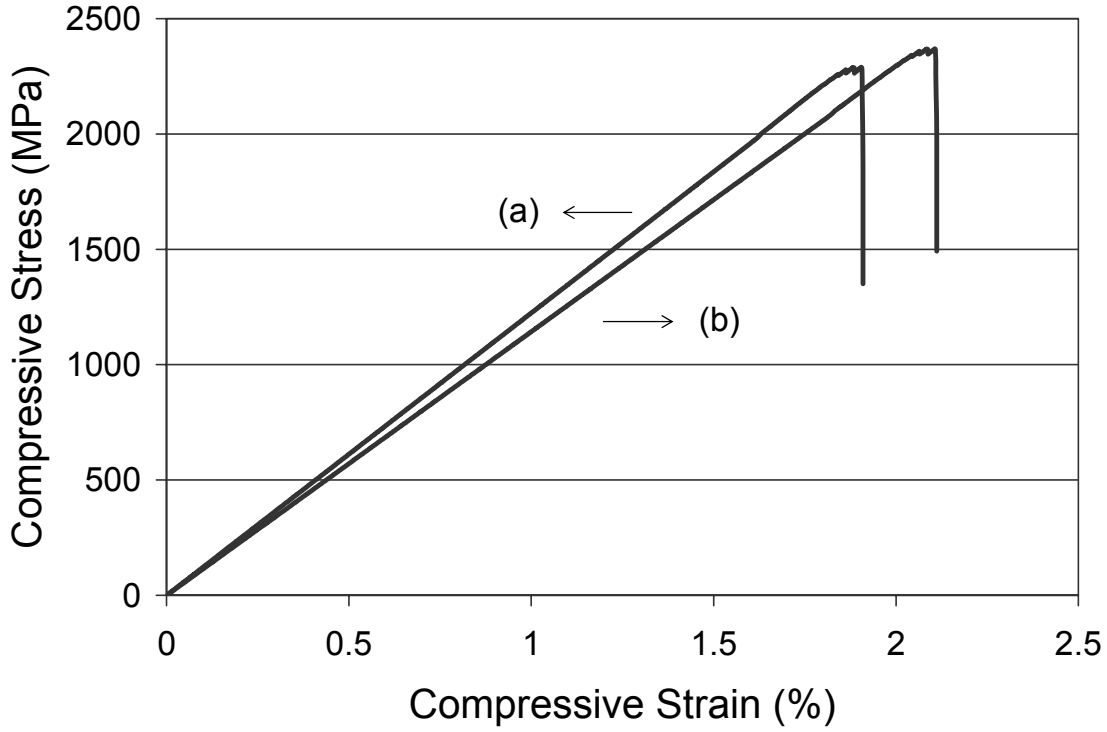

Fig 2.7 Compressive stress vs. strain curves of two selected alloys: (a) $Ni_{40}Cu_5Ti_{16.5}Zr_{28.5}Al_{10}$; and (b) $Ni_{45}Ti_{20}Zr_{25}Al_{10}$

Fig 2.7 presents the compressive stress vs. strain curves for two selected alloys. The slopes have been calibrated using the Young's modulus data measured from acoustic experiments. The strength data obtained from these compression tests are included in Table 2.2. These alloys have quite high fracture strength (~2.3-2.4 GPa). The quaternary alloy, $Ni_{45}Ti_{20}Zr_{25}AL_{10}$, has a slightly higher strength than the quinary alloys (e.g., RAG2). This is associated with the small drop in T_g caused by the addition of Cu (see Table 2.1). It is noteworthy that these alloys roughly obey the theoretical relation between Vicker's hardness and strength: $\sigma \sim 3*H_v$ (H_v in Kg/mm^2, σ in MPa) for isotropic materials. Significantly premature failure known for silica glass and some Ni-based BMG's [17] does not happen to these alloys.

2.4 Conclusions

The formation and properties of a new series of Ni-based bulk glass-forming alloys with formula $Ni_xCu_{a-x}Ti_yZr_{b-y}Al_{10}$ (a~b~45, in at.%) are reported which have a critical casting thickness ranging from 2 mm to 5 mm. The best GFA appears around x=40, y=16.5, a=b=45. These new amorphous alloys exhibit high thermal stabilities (ΔT ~40-50 K) and excellent mechanical properties (e.g., σ_f ~2.3-2.4 GPa). Small amount Si-addition is found to enhance the glass-forming abilities and the thermal stabilities of these alloys. The GFA and ΔT of some quaternary alloys are found not to be in agreement with each other. The glass forming abilities reported here may be the highest ever obtained for Ni-based alloys. Meanwhile, the all-metallic compositions endow these present Ni-based BMG's with excellent manufacturability.

References

[1] A. Peker and W. L. Johnson, Appl. Phys. Lett. **63**, 2342 (1993).

[2] A. Inoue and T. Zhang, Mater. Trans. JIM **37**, 185 (1996).

[3] A. Inoue, T. Nakamura, T. Sugita, T. Zhang and T. Masumoto, Mater. Trans. JIM **34**, 351 (1993).

[4] Z. P. Lu, Y. Li, S. C. Ng and Y. P. Feng, J. Non-Cryst. Solids **252**, 601 (1999).

[5] A. Inoue, A. Kato, T. Zhang, S. G. Kim and T. Masumoto, Mater. Trans. JIM **32**, 609 (1991).

[6] X. Wang, E. Yoshii, A. Inoue, Y. H. Kim and I. B. Kim, Mater. Trans. JIM **40**, 1130 (1999).

[7] S. Yi, J. K. Lee, W. T. Kim and D. H. Kim, J. Non-Cryst. Solids **291**, 132 (2001).

[8] T. Zhang and A. Inoue, Mater. Trans. JIM **43**, 708 (2002).

[9] H. Choi-Yim, D. H. Xu and W. L. Johnson, Appl. Phys. Lett. **82**, 1030 (2003).

[10] D. H. Xu, G. Duan, W. L. Johnson and C. Garland, Acta Mater. **52**, 3493 (2004).

[11] A. Inoue, Acta Mater. **48**, 279 (2000).

[12] T. A. Waniuk, J. Schroers, W. L. Johnson, Appl. Phys. Lett. **78**, 1213 (2001).

[13] Z. P. Lu, Y. Li and S. C. Ng, J. Non-Cryst. Solids **270**, 103 (2000).

[14] Z. P. Lu and C. T. Liu, Acta Mater. **50**, 3501 (2002).

[15] D. Turnbull, Contemp. Phys. **10**, 473 (1969**)**.

[16] C. T. Liu, M. F. Chisholm, M. K. Miller, Intermetallics **10**, 1105 (2002).

[17] H. Choi-Yim, D.H. Xu, unpublished work. We found Ni-Nb-Sn alloys reported in Ref. [9] fail prematurely; the apparent strength obtained from compression tests is quite lower than expected values.

Chapter 3

Formation of bulk metallic glasses in binary Cu-Zr and Cu-Hf systems

3.1 Introduction

As we have discussed earlier (Section 1.4.2) in Chapter 1, the sudden improvement in the glass-forming ability (GFA) from the early poor metallic glass formers (before the end of the 1980's) to the first bulk metallic glasses (Zr- [1,2], La- [3,4], and Mg- [5] based, found at the end of the 1980's and the beginning of the 1990's), and the historical fact that the former were mostly binary alloys while the latter were invariantly multi-component alloys, have led to an impression that good glass-forming ability belongs solely to multi-component systems. In fact, containing at least three elements has long been considered a 'must' rule for BMG formation [6].

Why should binary alloys so distinctly differ from multi-component alloys in terms of glass-forming ability? Inoue [6] did not give an answer because nobody (including himself) even asked this question. It was just taken for granted that bulk glass formation is solely the privilege of multi-component alloys. Is the answer to this question important? Yes, because a 'binary bulk metallic glass,' if it exists, would be an excellent subject for theoretical studies on the fundamental problem of glass formation, since it possesses both the simplicity of binary alloys and the good glass forming ability of multi-component alloys. On the other hand, from an engineering point of view, such a binary bulk metallic glass might provide important guidance for the search for extremely good GFA and might improve the current alloy developing efficiency considerably.

Aimed to find the answer to the above question, and to save possibly innocent binary alloys from a possibly wrong conviction, I started alone the search for binary bulk metallic glasses at Caltech. This search turned out to be fruitful, with two binary BMG systems (namely, Cu-Zr and Cu-Hf) and three 2 mm thick BMG alloys (namely, $Cu_{64}Zr_{36}$, $Cu_{46}Zr_{54}$, $Cu_{66}Hf_{34}$) discovered[†].

3.2 Experimentals

The alloy compositions studied are $Cu_{100-x}Zr_x$ ($34 \leq x \leq 75$) and $Cu_{100-x}Hf_x$ ($30 \leq x \leq 50$) in Cu-Zr and Cu-Hf system[‡], respectively. The sample preparation and characterization methods are basically the same as described in Chapter 2 (Section 2.2) except that a Bruker AXS diffractometer with a Cu- Kα source was used for X-ray structural analyses instead of the Inel with a Co Kα source. All of the studied alloys were subjected to copper mold casting and subsequent X-ray and DSC scannings. The three best compositions (with a critical casting thickness of 2 mm) were further examined using TEM. The mechanical properties of these three best alloys were then measured.

3.3 Results and Discussion

3.3.1 Glass-forming abilities

Cu-Zr system was once among the most intensively studied binary metallic glass systems before any BMG was reported (see, e.g., [10-13]). However, since the discovery of multi-

[†] Part of these results has been published in Ref. [7-9].
[‡] In fact, quite a number of alloys in other binary systems (such as Ti-Cu, Zr-Ni, etc.) were also studied in this research, but no bulk glasses (defined by a critical casting thickness of at least 1 mm) were found except in the Cu-Zr and Cu-Hf systems to be discussed here.

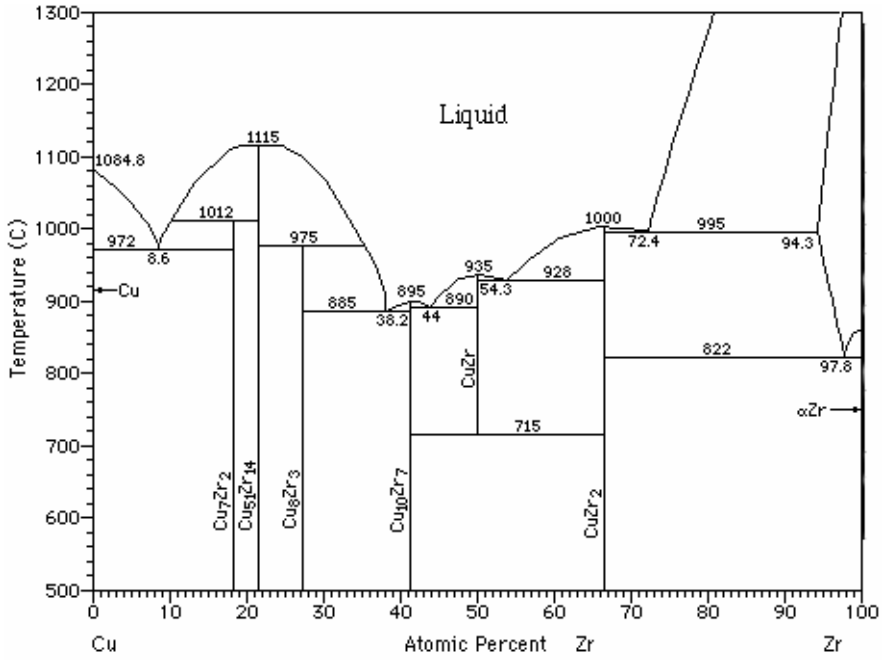

Fig 3.1 Binary Cu-Zr phase diagram (reproduced from Ref. [17])

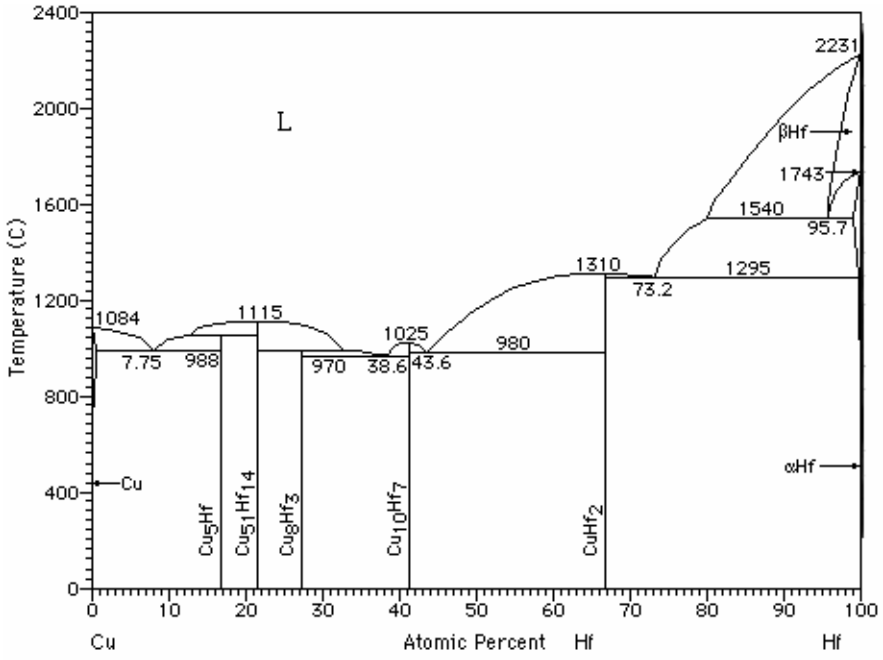

Fig 3.2 Binary Cu-Hf phase diagram (reproduced from Ref. [17])

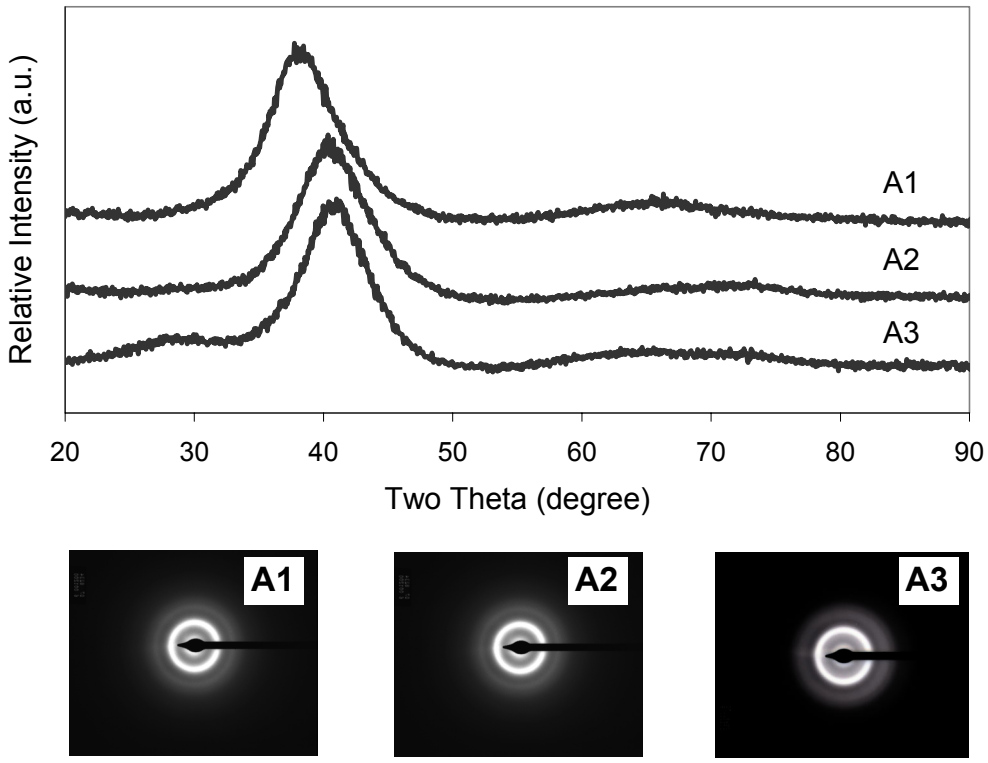

Fig 3.3 X-ray (taken with a Cu Kα source) and electron diffraction patterns of $Cu_{46}Zr_{54}$ (A1), $Cu_{64}Zr_{36}$(A2) and $Cu_{66}Hf_{34}$ (A3)

component BMG alloys in the late 1980's and early 1990's, this system -- like other binary systems -- has received dramatically reduced attention, although occasionally, a few studies on this system can still be found in the literature (e.g., [14-15]). The reason behind this is that binary alloy systems including Cu-Zr were considered impossible to form bulk metallic glasses and thus, were thought not likely to have any practical impact. According to a recent paper [16] by Inoue and his colleagues, "it is well known that no bulk glassy alloy is formed in Cu-Zr binary alloys by the copper mold casting method." Nevertheless, no systematic studies (directly by copper mold casting method) could be found on the glass-forming abilities in this as well as other binary systems to support Inoue's conclusion. This present research is most likely the first study of this type.

The alloy compositions were selected around deep eutectics. According to Turnbull's T_{rg} ($=T_g/T_l$) rule [18], the deep eutectic zone where high T_{rg} values may occur (due to low T_l) is probably also the place where good glass-forming ability would appear. On the other hand, as was discussed in Chapter 1 (Section 1.4.1), the T_{rg} rule may not be able to exactly pinpoint the best glass forming composition. Therefore, one should examine a range of compositions instead of the lowest liquidus point (i.e., x=38.2 in Cu-Zr system and x=38.6 in Cu-Hf system) only.

Figure 3.3 shows the X-ray and electron diffraction patterns taken from the cross sections of 2 mm thick cast strips of the three best glass formers in Cu-Zr and Cu-Hf systems discovered in this study (namely, $Cu_{64}Zr_{36}$, $Cu_{46}Zr_{54}$, $Cu_{66}Hf_{34}$). It can be seen that the diffraction patterns of these 2 mm strips only consist of diffuse maxima (X-ray) or diffuse halo rings (electron diffraction) without any sharp Bragg peaks (or rings). Therefore, both

of these two diffraction methods prove that the 2 mm strips are all fully amorphous within the instruments' detection limits.

Varying the alloy composition by even 1 or 2 at.% on either side of these three best glass formers results in a lower glass-forming ability. Take the alloy $Cu_{64}Zr_{36}$ as an example: to its left side on the phase diagram (Fig 3.1), reducing Zr content from 36% to 34% leads to a dramatic decrease in the critical casting thickness (from 2mm to below 0.5 mm). This is evidenced by the XRD pattern taken from the 0.5 mm thick cast strip of the alloy $Cu_{66}Zr_{34}$, which is shown in Fig 3.4. A couple of sharp Bragg peaks are superimposed on the diffuse diffraction background of this alloy, indicating that the 0.5 mm thick strip of $Cu_{66}Zr_{34}$ is already partially crystallized. Therefore, one expects that the critical casting thickness required to get a fully amorphous structure of this alloy is below 0.5 mm. On the right side of $Cu_{64}Zr_{36}$, all the studied alloys exhibit a fully amorphous structure at a 0.5 mm thickness, as can be seen from Fig 3.4. However, the 2 mm thick strips of $Cu_{61.8}Zr_{38.2}$ and $Cu_{60}Zr_{40}$ are significantly crystallized, as evidenced by the fairly well-developed sharp Bragg peaks appearing on their XRD patterns (shown in Fig 3.5). Apparently, the critical casting thickness of both $Cu_{61.8}Zr_{38.2}$ and $Cu_{60}Zr_{40}$ is lower than 2 mm (most likely ~ 1 mm, since their 0.5 mm thick strips are fully amorphous, according to XRD patterns in Fig 3.4).

3.3.2 Thermal analyses with DSC

Thermal analyses were performed using DSC aimed to measure the thermal properties, monitor the glass transition and crystallization behaviors of these binary BMGs, and to understand the tendencies in their glass-forming abilities.

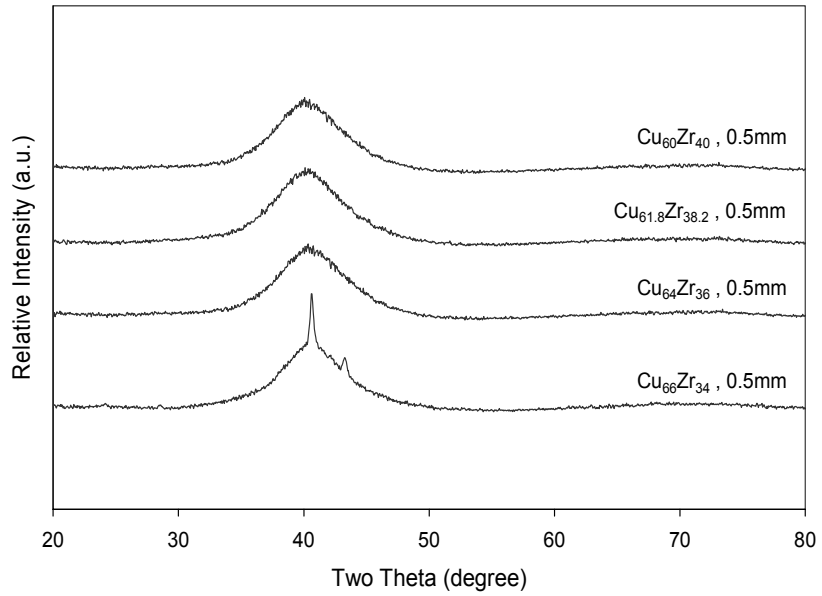

Fig 3.4 XRD patterns taken from 0.5 mm thick strips of $Cu_{100-x}Zr_x$ (x=34, 36, 38.2, 40 at.%) using a Cu-Kα source

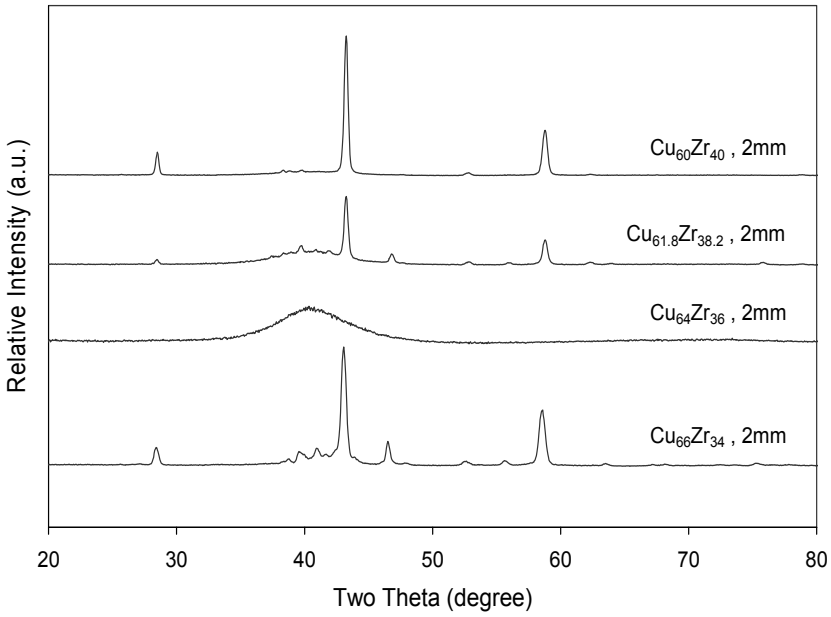

Fig 3.5 XRD patterns taken from the cross sections of the 2mm thick cast strips of $Cu_{100-x}Zr_x$ (x=34, 36, 38.2, 40 at.%) using a Cu-Kα source

Table 3.1 lists the thermal properties of the three best glass formers: $Cu_{64}Zr_{36}$, $Cu_{46}Zr_{54}$, and $Cu_{66}Hf_{34}$. The reduced glass transition temperatures (T_{rg}) of these three alloys are all on the high side (close to 2/3), according to Turnbull's model [18]. Besides, these alloys also exhibit a fairly wide undercooled liquid region (ΔT) which means they are quite stable against crystallization upon heating.

Nevertheless, neither of these two parameters can be used to explain the exact tendencies in the glass-forming abilities in these two binary systems. Still, we take the alloys around $Cu_{64}Zr_{36}$ (i.e., the alloy series $Cu_{100-x}Zr_x$ (x=34, 36, 38.2, 40 at.%)) as examples. Their T_g and T_{x1} values were all extracted from their DSC scans which are shown in Fig 3.6. Then, both the ΔT and T_{rg}[†] values are calculated and plotted against x as shown in Fig 3.7. One can see that these two parameters have quite similar trends within this alloy series. They both increase when x changes from 34 to 38.2, and decrease when x goes from 38.2 to 40, but neither of them assumes its maximum at x=36 which corresponds to the best GFA. This once again proves that solely relying on these empirical parameters (rules) may not be a good choice, especially when fine optimization of glass-forming composition within a given system is concerned.

Table 3.1 Thermal properties of three best glass formers in Cu-Zr and Cu-Hf systems

Alloy	T_g (K)	T_{x1} (K)	T_l (K)	$\Delta T = T_{x1} - T_g$ (K)	$T_{rg} = T_g/T_l$	Critical casting thickness (mm)
$Cu_{46}Zr_{54}$	696	746	1201	50	0.58	2
$Cu_{64}Zr_{36}$	787	833	1233	46	0.64	2
$Cu_{66}Hf_{34}$	787	841	1263	54	0.62	2

[†] For the calculations of T_{rg}, the liquidus temperatures were taken directly from the phase diagrams (i.e., Fig 3.1 and 3.2, provided in Ref. [17]).

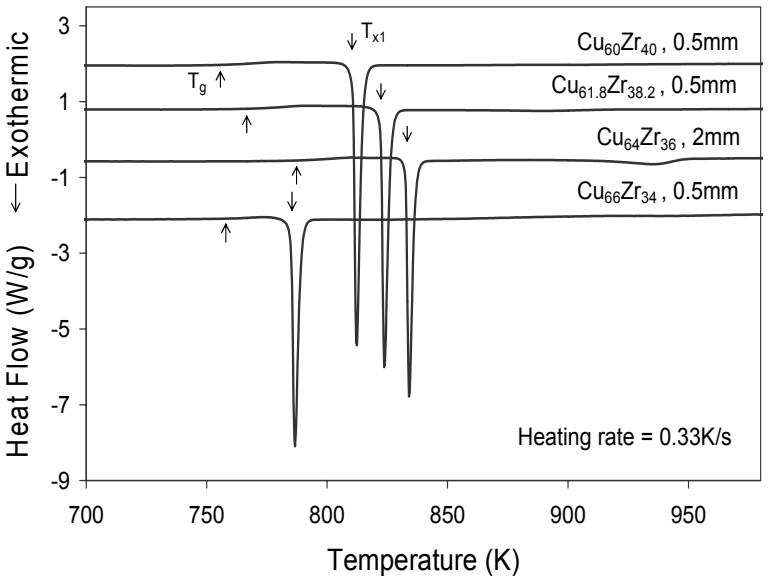

Fig 3.6 DSC scans of the 0.5mm thick strips of $Cu_{60}Zr_{40}$, $Cu_{61.8}Zr_{38.2}$, and $Cu_{66}Zr_{34}$; and the 2mm thick strip of $Cu_{64}Zr_{36}$ obtained at a heating rate of 0.33K/s

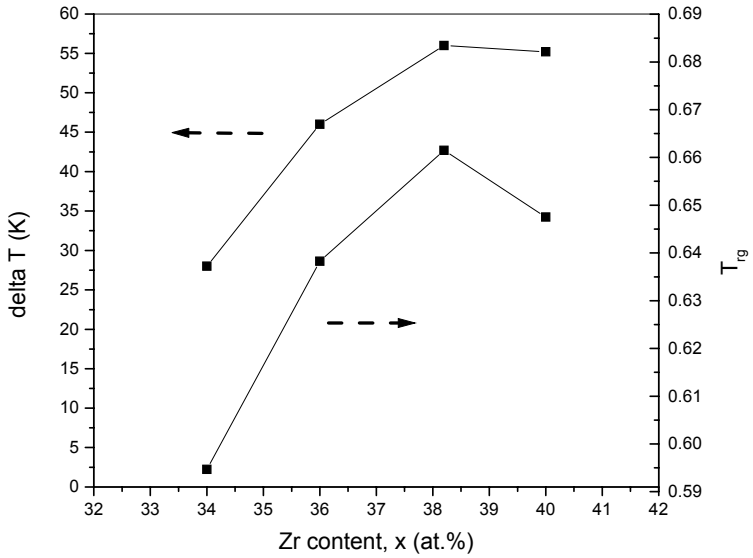

Fig 3.7 Variations of ΔT and T_{rg}, with respect to Zr content x in alloy series $Cu_{100-x}Zr_x$ (x=34, 36, 38.2, 40 at.%)

3.3.3 Mechanical properties of the three best glass formers

The mechanical properties of the three best glass formers -- $Cu_{64}Zr_{36}$, $Cu_{46}Zr_{54}$, and $Cu_{66}Hf_{34}$ -- were measured using the methods described in Chapter 2 (Section 2.2). The obtained data are summarized in Table 3.2. In addition, the compressive stress vs. strain curves of these alloys obtained at a strain rate of ~$4x10^{-4}$ s^{-1} at room temperature are given in Fig 3.8. From both Table 3.2 and Fig 3.8, one can see that the two alloys rich in Cu, namely, $Cu_{64}Zr_{36}$ and $Cu_{66}Hf_{34}$ both exhibit yielding strength exceeding 2 GPa. The one rich in Zr (i.e., $Cu_{46}Zr_{54}$), although yielding at a lower stress, has better ductility as evidenced by its distinct plastic strain ~1.1% on the stress-strain curve.

Table 3.2 Mechanical properties of three best glass formers in Cu-Zr and Cu-Hf systems

Alloy	Density (g/cc)	Vicker's Hardness (Kg/mm^2)	Young's Mod. (GPa)	Shear Mod. (GPa)	Poisson Ratio	Yielding Strength (GPa)	Fracture Strength (GPa)	Yielding Strain (%)	Plastic Strain (%)
$Cu_{46}Zr_{54}$	7.3	698	83	31	0.35	1.4	1.7	1.7	1.1
$Cu_{64}Zr_{36}$	7.9	742	92.3	34	0.34	2	2	2.2	~0
$Cu_{66}Hf_{34}$	11.4	779	111	40	0.37	2.1	2.1	1.86	~0

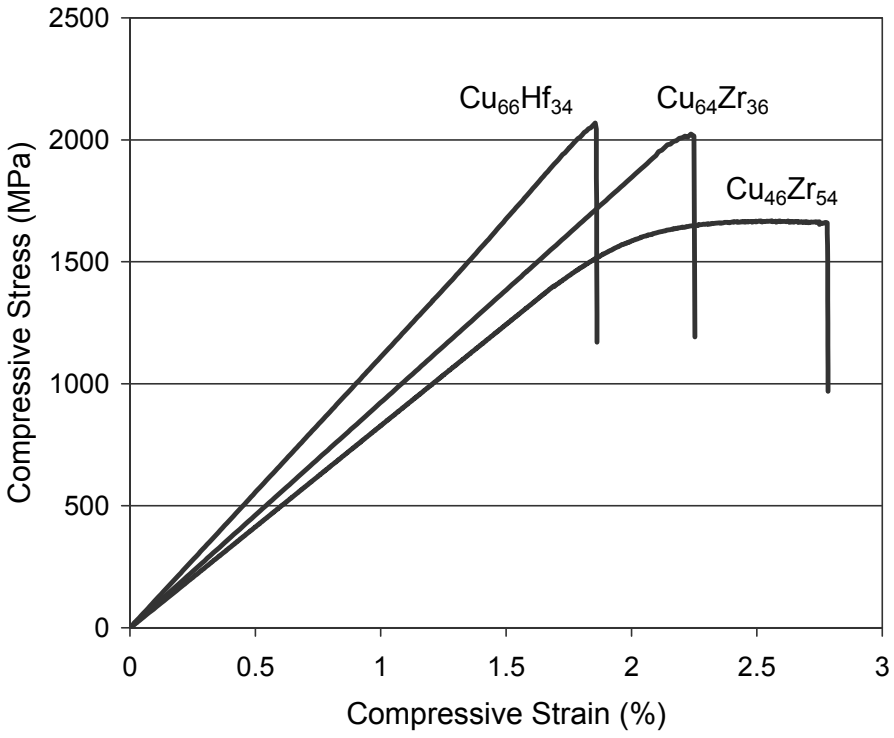

Fig 3.8 Compressive stress vs. strain curves of the three best glass formers in Cu-Zr and Cu-Hf systems obtained at a strain rate of ~$4x10^{-4}$ s^{-1} at room temperature

3.4 Conclusions

For the first time, glass-forming abilities of binary alloys in Cu-Zr and Cu-Hf systems were systematically studied using the copper mold casting method. It was found that some of the binary alloys can form bulk metallic glasses, even with a critical casting thickness up to 2 mm. These results have proven that the previously well-accepted 'three component rule' for BMG formation is actually wrong. There may not be a strict boundary between the glass-forming abilities of binary alloys and those of multi-component alloys, although more multi-component alloys have been seen to form BMGs. It was also found that the two empirical factors for evaluating glass-forming ability (i.e., ΔT and T_{rg}), although being able to explain to some extent the good glass-forming abilities of the two binary alloy systems as a whole, can't yet be used to pinpoint exactly the best glass-forming compositions in these systems. The thermal and mechanical properties of the three best glass-formers in the two systems were measured and reported in this chapter. Finally, the three best glass-formers in the two studied systems (namely, $Cu_{64}Zr_{36}$, $Cu_{46}Zr_{54}$, and $Cu_{66}Hf_{34}$) provide an exceptional combination of chemical simplicity and good glass-forming ability and thus, may become special subjects for simulation or modeling of BMG formation.

References

[1] A. Peker and W. L. Johnson, Appl. Phys. Lett. **63**, 2342 (1993).

[2] A. Inoue and T. Zhang, Mater. Trans. JIM **37**, 185 (1996).

[3] A. Inoue, T. Nakamura, T. Sugita, T. Zhang and T. Masumoto, Mater. Trans. JIM **34**, 351 (1993).

[4] Z. P. Lu, Y. Li, S. C. Ng and Y. P. Feng, J. Non-Cryst. Solids **252**, 601 (1999).

[5] A. Inoue, A. Kato, T. Zhang, S. G. Kim and T. Masumoto, Mater. Trans. JIM **32**, 609 (1991).

[6] A. Inoue and A. Takeuchi, Mater. Trans. **43**, 1892 (2002).

[7] D. H. Xu, B. Lohwongwatana, G. Duan, W. L. Johnson and C. Garland, Acta Mater. **52**, 2621 (2004).

[8] G. Duan, D. H. Xu and W. L. Johnson, Metall. Mater. Trans. A. **36A**, 455 (2005).

[9] D. H. Xu, G. Duan and W. L. Johnson, Phys. Rev. Lett. **92**, 245504 (2004).

[10] J. Chevrier, Solid State Commun. **65**, 1461 (1988).

[11] A. Sadoc, Y. Calvayrac, A. Quivy, M. Harmelin and A. M. Flank, J. Non-Cryst. Solids **65**, 109 (1984).

[12] E. Kneller, Y. Khan and U. Gorres, Z. Metallkd. **77**, 43 (1986).

[13] E. Kneller, Y. Khan and U. Gorres, Z. Metallkd. **77**, 153 (1986).

[14] B. C. Anusionwu and G. A. Adebayo, J. Alloys Comp. **329**, 162 (2001).

[15] M. H. Braga, L. F. Malheiros, F. Castro and D. Soares, Z. Metallkd. **89**, 541 (1998).

[16] A. Inoue and W. Zhang, Mater. Trans. JIM **43**, 2924 (2002).

[17] *Binary Alloy Phase Diagrams*, 2nd ed., T. B. Massalski, ed. (ASM International, Metals Park, OH, 1990).

[18] D. Turnbull, Contemp. Phys. **10**, 473 (1969).

Chapter 4

A generalized model for the critical-value problem of nucleation

4.1 Introduction[†]

As we have seen in Chapter 1, crystal nucleation is an important issue related to (metallic) glass formation. Nucleation is generally classified into two categories: homogeneous nucleation and heterogeneous nucleation. The former refers to cases in which there are no extrinsic nucleating agents while the latter is influenced by such agents. In Chapter 1, we considered only homogeneous nucleation. However, in more cases, nucleation takes place in a heterogeneous manner.

The existing theory for heterogeneous nucleation is based mainly on the large-wall assumption in which the size of the extrinsic agent is taken as infinity. The solution to this problem can be found in many textbooks (e.g., [1]) as follows:

$$\begin{aligned} r_c^{het} &= \frac{2\sigma}{G} \\ E_c^{het} &= \frac{16\pi}{3}\frac{\sigma^3}{G^2} f^{het}(\theta) \\ f^{het}(\theta) &= [2-3\cos\theta+\cos^3\theta]/4 \end{aligned} \tag{4.1}$$

where θ is the contact angle between the nucleus and the extrinsic agent, σ is the interfacial energy per unit area (or, the interfacial tension) between the new phase (i.e., the nucleus) and the parental phase, and G is the Gibbs free energy difference per unit

[†] The content of this chapter has been accepted for publication in Phys. Rev. B (2005).

volume between the two phases. This solution states that in order for a small nucleus to grow from the parental phase, the size of the nucleus (r) and the energy associated with the formation of the nucleus (E) have to exceed the critical value r_c, and E_c determined by Eq. (4.1), respectively. By comparing this heterogeneous solution with the homogeneous solution given in Chapter 1 by Eq. (1.14), one can find that although the critical size of the nucleus r_c is the same for the two cases, the critical energy barrier E_c differs by the factor $f^{het}(\theta)$, given as part of Eq. (4.1), i.e.,

$$E_c^{het} = E_c^{\hom} f^{het}(\theta) \tag{4.2}$$

By plotting $f^{het}(\theta)$ (as shown in Fig 4.1), one notices that $f^{het}(\theta)$ takes on a value between 1 and 0, depending on the contact angle θ. If θ is 0, E_c^{het} is zero; if θ is π (i.e., 180°), $E_c^{het} = E_c^{\hom}$; and if $0 < \theta < \pi$, $E_c^{het} < E_c^{\hom}$. Therefore, unless the contact angle is π, the critical energy barrier for large-wall heterogeneous nucleation is always lower than for homogeneous nucleation. This model explains why heterogeneous nucleation is preferred most of the time if a large extrinsic wall exists.

Nevertheless, in a large variety of cases such as the formation of rain droplets from clouds or the nucleation of crystals from the interior of small-particle-bearing liquids, the assumptions adopted in the derivation of the above two classical solutions (i.e., a super clean parental phase for the homogeneous case, or a large extrinsic wall for the heterogeneous case) are not well satisfied, and consequently, these solutions may not provide precise descriptions of such cases.

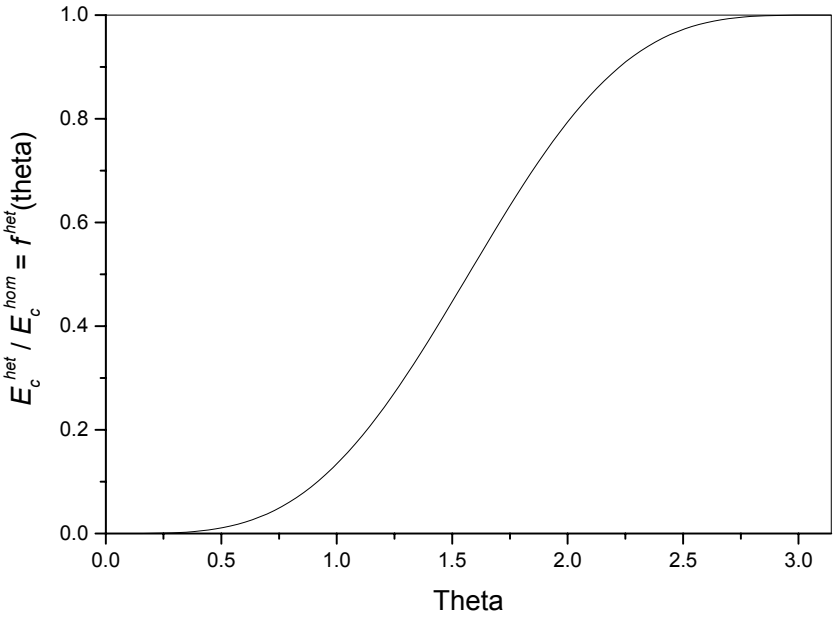

Fig 4.1 The geometric factor as a function of contact angle θ in the large-wall heterogeneous solution

In the field of metallic glass, it has been experimentally observed that the glass-forming ability (GFA) of an alloy upon cooling from its molten state is strongly influenced by the nucleating effect of the finite-sized impurities buried in the alloy melt. When the impurities are either fluxed [2,3] or deactivated [4], the undercooling and GFA of the alloy can be improved dramatically. However, it is still not clear exactly how these finite-sized impurity particles affect the nucleation process and how their effects can be carefully controlled by processing methods such as fluxing and microalloying. To help answer these questions, I present in this chapter a generalized geometric model for the critical problem of nucleation based on a finite-sized nucleating agent, then derive the exact solution and discuss its physical implications.

4.2 Model construction

Fig 4.2 (a) illustrates the geometric construction for the new model, where a nucleus (N) forms at the interface between the parental phase (P) and a finite-sized nucleating agent (A). O_1 and O_2 are the spherical centers of N and A, respectively. S is a joint where the three phases, P, N, and A, meet each other. Fig 4.2 (b) is an illustration of the mechanical equilibrium at S, in which σ, σ_{PA} and σ_{NA} denote the interfacial tensions between P and N, P and A, and N and A, respectively. In both figures, θ is the contact angle between N and A. Besides θ, we introduce another important angle φ, i.e., $\angle SO_2O_1$, to relate the radius of A (R, i.e., SO_2) with that of N (r, i.e., SO_1).

4.3 Model solution and interpretation

With the above construction and denotations, it is trivial to obtain the following expressions:

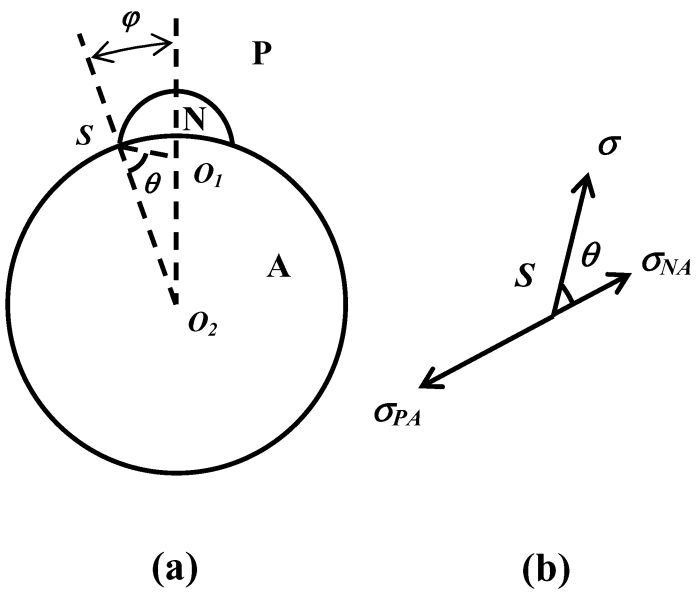

Fig 4.2 (a) the geometric construction for the generalized nucleation model; (b) an illustration of the mechanical equilibrium at point *S* in part (a)

1. The interfacial area (I.A.) between P and N (from Fig 4.2 (a)):

$$I.A._{PN} = 2\pi r^2[1-\cos(\varphi+\theta)] \tag{4.3}$$

2. The interfacial area between N and A (from Fig 4.2 (a)):

$$I.A._{NA} = 2\pi R^2(1-\cos\varphi) \tag{4.4}$$

3. The volume of N (from Fig 4.2 (a)):

$$V = \frac{\pi}{3}r^3[2-3\cos(\varphi+\theta)+\cos^3(\varphi+\theta)] - \frac{\pi}{3}R^3(2-3\cos\varphi+\cos^3\varphi) \tag{4.5}$$

4. The interconnection among *r, R,* φ and θ (from triangle SO_1O_2 in Fig 4.2 (a)):

$$\frac{r}{\sin\varphi} = \frac{R}{\sin(\varphi+\theta)} \tag{4.6}$$

5. The interconnection among σ, σ_{PA},σ_{NA} and θ (from Fig 4.2 (b)):

$$\sigma_{PA} - \sigma_{NA} = \sigma\cos\theta \tag{4.7}$$

Therefore, the energy change associated with the formation of nucleus N is: (*G* as defined earlier)

$$\begin{aligned} E &= \sigma\times I.A._{PN} + (\sigma_{NA}-\sigma_{PA})\times I.A._{NA} - G\times V \\ &= \sigma\times I.A._{PN} - \sigma\cos\theta\times I.A._{NA} - G\times V \\ &= E_1 - E_2 \end{aligned} \tag{4.8},$$

where,

$$E_1 = 2\pi\sigma r^2[1-\cos(\varphi+\theta)] - 2\pi\sigma R^2\cos\theta(1-\cos\varphi) \tag{4.9},$$

and

$$E_2 = \frac{\pi}{3}Gr^3[2-3\cos(\varphi+\theta)+\cos^3(\varphi+\theta)] - \frac{\pi}{3}GR^3(2-3\cos\varphi+\cos^3\varphi) \tag{4.10}.$$

For a given system, we have fixed *R* and θ. From Eqn. (4.6), we get

$$\frac{dr}{d\varphi}=\frac{R\sin\theta}{\sin^2(\varphi+\theta)} \tag{4.11}$$

From Eqn. (4.9), (4.6) and (4.11), we get

$$\begin{aligned}
&\frac{dE_1}{dr}=2\pi\sigma R^2\frac{d}{dr}\{\frac{\sin^2\varphi}{\sin^2(\varphi+\theta)}[1-\cos(\varphi+\theta)]-\cos\theta(1-\cos\varphi)\}\\
&=2\pi\sigma R^2\frac{d\varphi}{dr}\times\frac{d}{d\varphi}[\frac{\sin^2\varphi}{1+\cos(\varphi+\theta)}-\cos\theta(1-\cos\varphi)]\\
&=2\pi\sigma R\frac{\sin^2(\varphi+\theta)}{\sin\theta}\times\sin\varphi\times\{\frac{2\cos\varphi}{1+\cos(\varphi+\theta)}+\frac{\sin\varphi\sin(\varphi+\theta)}{[1+\cos(\varphi+\theta)]^2}-\cos\theta\}\\
&=2\pi\sigma r\sin(\varphi+\theta)\frac{1-\cos^2(\varphi+\theta)}{\sin\theta}\times\{\frac{2\cos\varphi}{1+\cos(\varphi+\theta)}+\frac{\sin\varphi\sin(\varphi+\theta)}{[1+\cos(\varphi+\theta)]^2}-\cos\theta\}\\
&=2\pi\sigma r\frac{1-\cos(\varphi+\theta)}{\sin\theta}\times\{2\cos\varphi\sin(\varphi+\theta)+\sin\varphi[1-\cos(\varphi+\theta)]-\cos\theta\sin(\varphi+\theta)[1+\cos(\varphi+\theta)]\}\\
&=2\pi\sigma r\frac{1-\cos(\varphi+\theta)}{\sin\theta}\times\{2[\sin\theta+\sin\varphi\cos(\varphi+\theta)]+\sin\varphi[1-\cos(\varphi+\theta)]-\cos\theta\sin(\varphi+\theta)[1+\cos(\varphi+\theta)]\}\\
&=2\pi\sigma r\frac{1-\cos(\varphi+\theta)}{\sin\theta}\times\{2\sin\theta+\sin\varphi[1+\cos(\varphi+\theta)]-\cos\theta\sin(\varphi+\theta)[1+\cos(\varphi+\theta)]\}\\
&=2\pi\sigma r\frac{1-\cos(\varphi+\theta)}{\sin\theta}\times\{2\sin\theta-\sin\theta\cos(\varphi+\theta)[1+\cos(\varphi+\theta)]\}\\
&=2\pi\sigma r[2-3\cos(\varphi+\theta)+\cos^3(\varphi+\theta)]
\end{aligned} \tag{4.12}$$

From Eqn. (4.10) and (4.6) we get

$$\begin{aligned}
&\frac{dE_2}{dr}=\frac{\partial E_2}{\partial r}+\frac{\partial E_2}{\partial\varphi}\frac{d\varphi}{dr}\\
&=\pi Gr^2[2-3\cos(\varphi+\theta)+\cos^3(\varphi+\theta)]+\\
&\quad\frac{d\varphi}{dr}\times\{\frac{\pi}{3}Gr^3[3\sin(\varphi+\theta)-3\cos^2(\varphi+\theta)\sin(\varphi+\theta)]-\frac{\pi}{3}GR^3(3\sin\varphi-3\cos^2\varphi\sin\varphi)\}\\
&=\pi Gr^2[2-3\cos(\varphi+\theta)+\cos^3(\varphi+\theta)]+\pi G\frac{d\varphi}{dr}\times[r^3\sin^3(\varphi+\theta)-R^3\sin^3\varphi]\\
&=\pi Gr^2[2-3\cos(\varphi+\theta)+\cos^3(\varphi+\theta)]
\end{aligned} \tag{4.13}$$

Therefore, from Eqn. (4.8), (4.12) and (4.13), we have

$$\frac{dE}{dr} = \frac{dE_1}{dr} - \frac{dE_2}{dr}$$
$$= 2\pi\sigma r[2 - 3\cos(\varphi+\theta) + \cos^3(\varphi+\theta)] - \pi G r^2[2 - 3\cos(\varphi+\theta) + \cos^3(\varphi+\theta)]$$
$$= \pi r(2\sigma - Gr)[2 - 3\cos(\varphi+\theta) + \cos^3(\varphi+\theta)]$$

(4.14).

The critical condition is $\left.\frac{dE}{dr}\right|_{r_c} = 0$. Hence, we get

$$r_c = \frac{2\sigma}{G} \tag{4.15}.$$

It is clear that the critical diameter of the nucleus does not depend on either the contact angle θ or the nucleating-agent size *R*, and has the same value for the generalized case and for the two classical cases (i.e., $r_c = r_c^{\text{hom}} = r_c^{het}$).

To find out the critical energy barrier E_c, we first substitute r_c into Eqn. (4.9) and (4.10), and then into (4.8). We get

$$E_1\big|_{r_c} = 8\pi\frac{\sigma^3}{G^2}[1 - \cos(\varphi+\theta) - \frac{\sin^2(\varphi+\theta)}{\sin^2\varphi}\cos\theta(1-\cos\varphi)] \tag{4.16},$$

$$E_2\big|_{r_c} = \frac{8\pi}{3}\frac{\sigma^3}{G^2}[2 - 3\cos(\varphi+\theta) + \cos^3(\varphi+\theta) - \frac{\sin^3(\varphi+\theta)}{\sin^3\varphi}(2 - 3\cos\varphi + \cos^3\varphi)] \tag{4.17},$$

and

$$\begin{aligned} E_c &= E_1\big|_{r_c} - E_2\big|_{r_c} \\ &= \frac{16\pi}{3}\frac{\sigma^3}{G^2}g(R,\theta) \end{aligned} \tag{4.18},$$

where

$$g(R,\theta) = \frac{1}{2}[1 - \cos^3(\varphi+\theta) - 3\cos\theta\frac{\sin^2(\varphi+\theta)}{1+\cos\varphi} + \frac{\sin^3(\varphi+\theta)}{\sin^3\varphi}(2 - 3\cos\varphi + \cos^3\varphi)] \tag{4.19},$$

and $\varphi = \varphi(R,\theta)$ is determined by Eqn. (4.6), or explicitly,

$$\varphi = arc\cot(\frac{R/r_c - \cos\theta}{\sin\theta}) \tag{4.20}.$$

Fig 4.3 (a), (b) and (c) represent the 3D image and some 2D projected curves of this bivariate function $g(R,\theta)$ with R scaled by $r_c = \frac{2\sigma}{G}$. From these figures as well as from Eqn. (4.19) and (4.20), it can be seen that for any fixed contact angle θ (i.e., fixed type of nucleating agent), as the agent size R goes to 0 [5], $g(R,\theta)$ goes to 1, corresponding to E_c going to $E_c^{\hom} = \frac{16\pi}{3}\frac{\sigma^3}{G^2}$, which means nucleation occurs in a homogeneous manner in the limiting case where $R = 0$. Also, for any fixed θ, as R goes to $+\infty$, $g(R,\theta)$ goes to a constant value $g(+\infty,\theta)$. It is trivial to find the expression for $g(+\infty,\theta)$ through Eqn. (4.19) and (4.20) [5]:

$$\begin{aligned} g(+\infty,\theta) &= \frac{1}{2}(1-\cos^3\theta - \frac{3}{2}\cos\theta\sin^2\theta) \\ &= \frac{1}{4}(2-3\cos\theta+\cos^3\theta) \\ &= f^{het}(\theta) \end{aligned} \tag{4.21}.$$

Therefore, the classical heterogeneous solution (i.e., Eqn. (4.2)) actually describes only the limiting case of the current generalized model, where the agent size tends to infinity. Although this limiting solution may be at the same time a good estimate for $g(R,\theta)$ when R is significantly larger than the critical nucleus diameter r_c (by ~ two orders of magnitude or more according to Fig 4.3(b)), it can't be used to depict a large category of nucleation processes occurring at low 'undercoolings' of a parental phase [6]. This is because at low undercoolings, the Gibbs free energy difference between the parental

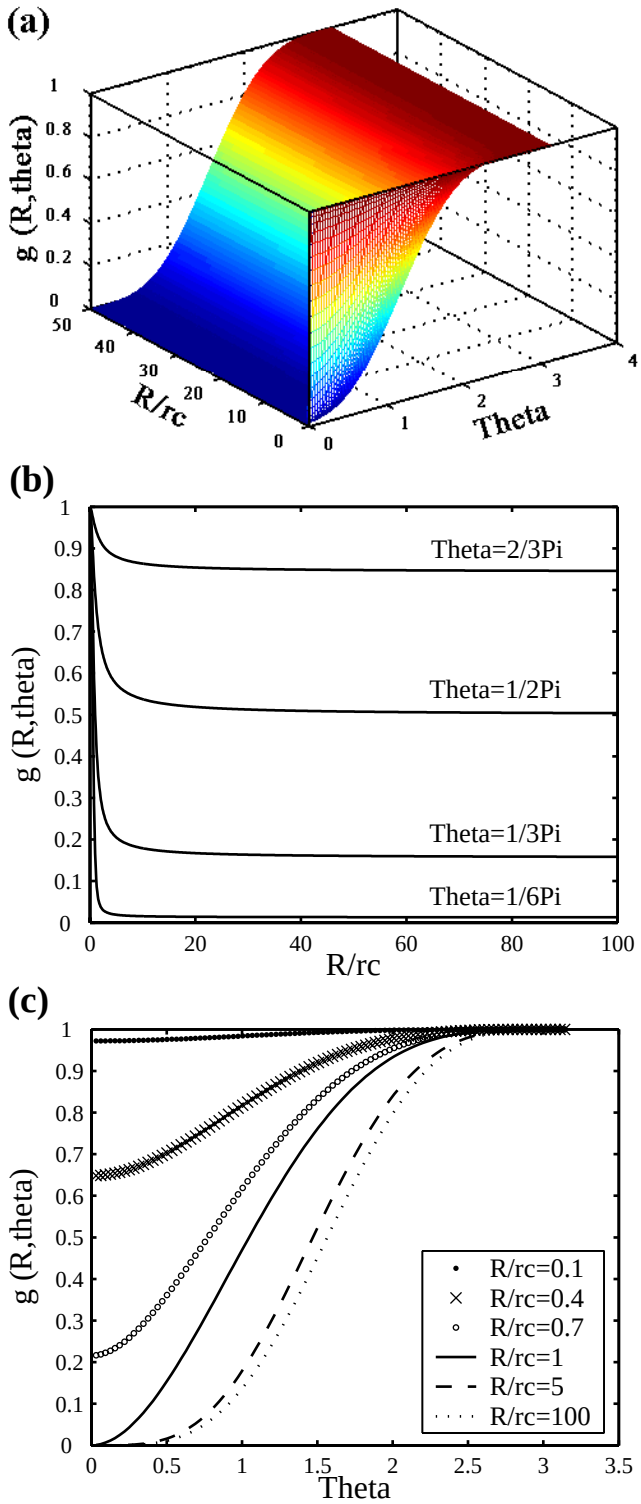

Fig 4.3 (a) 3D image of the bivariate function $g(R,\theta)$; (b) 2D plots of $g(R,\theta)$ vs. R/r_c at different values of θ; (c) 2D plots of $g(R,\theta)$ vs. θ at different values of R/r_c.

phase and the new phase is very small, and thus, the critical nucleus diameter is very large according to $r_c = \frac{2\sigma}{G}$, as a result of which a finite nucleating agent can't be readily considered significantly larger than r_c. Therefore, in such general cases, the present model should be considered.

Besides the nucleating-agent size effect, this generalized model also releases new information about the dependence of the critical energy barrier on the contact angle θ. The classical heterogeneous solution (i.e., Eqn. (4.1)) predicts that the critical energy barrier drops from E_c^{hom} to 0 as θ decreases from π to 0. However, in the present generalized model, the conclusion is somewhat different. For convenience sake, here we consider another form of Eqn. (4.19):

$$g(R,\theta) = \frac{1}{2}[1-\cos^3(\varphi+\theta) - 3(\frac{R}{r_c})^2\cos\theta(1-\cos\varphi) + (\frac{R}{r_c})^3(2-3\cos\varphi+\cos^3\varphi)] \qquad (4.22)$$

since we fix the value of R in order to study the contribution of varying θ. As can been seen from Fig 4.3 (c), as well as from Eqn. (4.20) and (4.22) [7], for any fixed R $(0 \le R < \infty)$, as θ tends to π, $g(R,\theta)$ always tends to 1, and thus, nucleation always tends to occur in a homogeneous manner. Nevertheless, as θ tends to 0, the value of $g(R,\theta)$ depends on whether $R \ge r_c$ or $R < r_c$. If $R \ge r_c$, $g(R,\theta)$ always tends to 0, meaning the nucleation energy barrier disappears at $\theta = 0$; if $R < r_c$, $g(R,\theta)$ tends to a finite value $g(R,0) = 1 - 3(\frac{R}{r_c})^2 + 2(\frac{R}{r_c})^3$ as determined by Eqn. (4.20) and (4.22). In the

latter case, the smaller the ratio $\frac{R}{r_c}$, the closer $g(R,0)$ is to 1 (i.e., the closer the nucleation process is to the homogeneous case, even though $\theta = 0$).

It is also noteworthy that the previously presumed relationship between the critical energy barrier (E_c) and the volumetric Gibbs free energy of the critical nucleus ($E_2\big|_{r_c}$): $E_c = \frac{1}{2} E_2\big|_{r_c}$ does not necessarily hold for a finite R in the present generalized model (see Eqn. (4.17-4.19)), although it is correct in the two limiting cases (i.e., when $R = 0$ or $R = +\infty$).

4.4 Conclusions

A generalized geometric model for the critical problem of nucleation has been established to account for the size effect of an extrinsic nucleating agent. The classical solutions to homogeneous and large-wall heterogeneous critical problems have been proven to be limiting cases of this generalized model. Since in many cases, the limiting conditions adopted in the derivations of the two classical solutions (i.e., a super clean parental phase for the homogeneous case, or a large extrinsic wall for the heterogeneous case) are not well satisfied, this present model is expected to provide a more complete and reliable description for general nucleation phenomena. Although the quantitative preciseness of this generalized model requires careful experimental verification in the future, yet this model clearly proves: 1). heterogeneous nucleation always has a critical energy barrier no larger (most of the time, lower) than does homogeneous nucleation regardless of the size

of the extrinsic nucleating agent; 2). the larger the extrinsic agent size (relative to the critical nucleus size) the lower the critical energy barrier for heterogeneous nucleation.

References

[1] D. A. Porter and K. E. Easterling, *Phase Transformations in Metals and Alloys*, 2nd Ed. (Chapman & Hall, London, 1992).

[2] H. W. Kui, A. L. Greer and D. Turnbull, Appl. Phys. Lett. **45**, 615 (1984).

[3] D. M. Herlach, D. Holland-Moritz, T. Schenk, K. Schneider, G. Wilde, O. Boni, J. Fransaer and F. Spaepen, J. Non-Cryst. Solids **250**, 271 (1999).

[4] Z. P. Lu, C. T. Liu and W. D. Porter, Appl. Phys. Lett. **83**, 2581 (2003).

[5] According to Eqn. (4.20), for a fixed θ ($0 \le \theta \le \pi$), R going to 0 is equivalent to φ going to π-θ, and R going to $+\infty$ is equivalent to φ going to 0.

[6] Here, 'undercooling' refers to the deviation from the thermodynamic equilibrium between the parental phase and the new phase such that the following discussion not only applies to the crystallization-of-liquid case, but also to most other cases.

[7] According to Eqn. (4.20), for any fixed R $(0 \le R < \infty)$, θ going to π is equivalent to φ going to 0. For a fixed R ($R > r_c$), θ going to 0 is equivalent to φ going to 0. For a fixed R ($R < r_c$), θ going to 0 is equivalent to φ going to π. If $R = r_c$, θ going to 0 is equivalent to φ going to $\pi/2$.

Chapter 5

Centimeter size BMG formation in Cu-Zr-Al-Y system

5.1 Introduction

In the last chapter, we saw that crystal nucleation may be enhanced by finite-sized extrinsic agents inside an alloy melt. Previous experiments [1] have shown that some oxide particles (e.g., Zirconium oxides) present in BMG alloys are among such effective nucleating agents. Therefore, the removal or deactivation of such oxide particles is expected to improve an alloy's glass-forming ability (GFA). For Pd-Cu-Ni-P alloys, B_2O_3 has been used to remove the oxide particles[†] and clean the molten alloys by a fluxing method [2]. However, this method can't be applied to alloy systems containing species (such as Zirconium) with higher oxygen affinity than boron because B_2O_3 may be chemically reduced by such species and then lose its fluxing function. It was then found that for such systems, heterogeneous nucleation may be restrained by chemically transforming the active oxides into a certain type of deactivated oxides. For example, by transforming detrimental Zirconium oxides into neutral Yttrium oxides, small amount yttrium addition to Fe- (containing Zr) and Zr- based amorphous alloys can alleviate the oxygen problems in these systems to a certain degree [3].

Meanwhile, in Chapter 3, we have reported the surprising discovery of bulk metallic glasses in binary Cu-Zr and Cu-Hf systems. $Cu_{46}Zr_{54}$ is one of the three best glass-forming compositions in these two systems which exhibit a critical casting thickness of

[†] and maybe other detrimental particles

2mm. The discovery of these binary BMGs strongly suggests that even higher GFA may be achievable in Cu-based alloys. On one hand, the further improvement of GFA may be realized by appropriately introducing additional alloying elements. As a matter of fact, Inoue et al. had reported earlier [4] that the critical casting thickness of certain ternary Cu-based alloys in Cu-Zr-Al system is ~3 mm. On the other hand, the GFA may be enhanced by deactivating detrimental Zr oxides. Based on these two considerations, I systematically examined the effects of Y doping on a ternary alloy, $Cu_{46}Zr_{47}Al_7$ (referred to as 'matrix alloy' in the following context). The results[†] show that the consequent Cu-based alloys, $Cu_{46}Zr_{47-x}Al_7Y_x$ ($0<x\leq10$, in at.%) possess unusually high GFA. The amorphous structure of a representative alloy, $Cu_{46}Zr_{42}Al_7Y_5$, can readily be obtained even when the casting diameter exceeds 1cm. The physical mechanism underlying the achievement of this unusual GFA is investigated by high temperature thermal analysis and TEM (Transmission Electron Microscopy), combined with EDS (Energy Dispersive X-ray Spectroscopy) and X-ray dot mapping techniques.

5.2 Experimentals

The samples were prepared by arc melting and subsequent copper mold casting, as described in Chapter 2 (Section 2.2). The copper molds used here have internal cylindrical cavities of diameters ranging from 2mm to 14mm. The transverse cross sections of the as-cast samples were analysed with X-ray diffraction (XRD) method using a Cu-Kα source. The glass transition and crystallization behaviors of amorphous samples were analyzed with a Perkin-Elmer DSC7 (Differential Scanning Calorimeter) which was

[†] A part of these results has been published in Ref. [5].

calibrated using Zn and Al standards. The melting behaviours of the alloys were analyzed with a Setaram DSC 2000K high temperature calorimeter at a heating rate of 0.33K/s. A Philips EM430 TEM operating at 300kV with an attached STEM unit and EDX detector was utilized for imaging, microstructural and chemical analysis. The TEM sections were prepared by ultramicrotomy and Mo grids were used to support the ultra-thin sections.

5.3 Results and Discussion

Fig 5.1(A) shows the pictures of three as-cast samples (S1, S2 and S3) of a representative alloy, $Cu_{46}Zr_{42}Al_7Y_5$, having a diameter of 10mm, 12mm and 14mm, respectively. Their as-cast surfaces all appear smooth and lustrous. No apparent volume reductions can be recognized on their surfaces, indicating there was no drastic crystallization during the formation of these samples. The XRD patterns of S1, S2 and S3 are presented in Fig 5.1(B). It can be seen that the pattern of S1 consists only of a series of broad diffraction maxima without any detectable sharp Bragg peaks, indicating that this 10mm diameter sample is fully amorphous. Moreover, the 12mm (S2) and 14mm (S3) samples, even though partially crystallized, still possess very large amorphous fractions judging from the broad diffraction background on their XRD patterns. This implies that the growth of the crystalline phase(s) in the supercooled liquid is quite sluggish, even when the sample size exceeds the critical value (~10mm) for the formation of a fully amorphous structure by ~40%. For a comparison, Fig 5.1(B) also presents the XRD patterns of 3mm (M1) and 4mm (M2) diameter rods of the matrix alloy, $Cu_{46}Zr_{47}Al_7$, from which it can be seen that

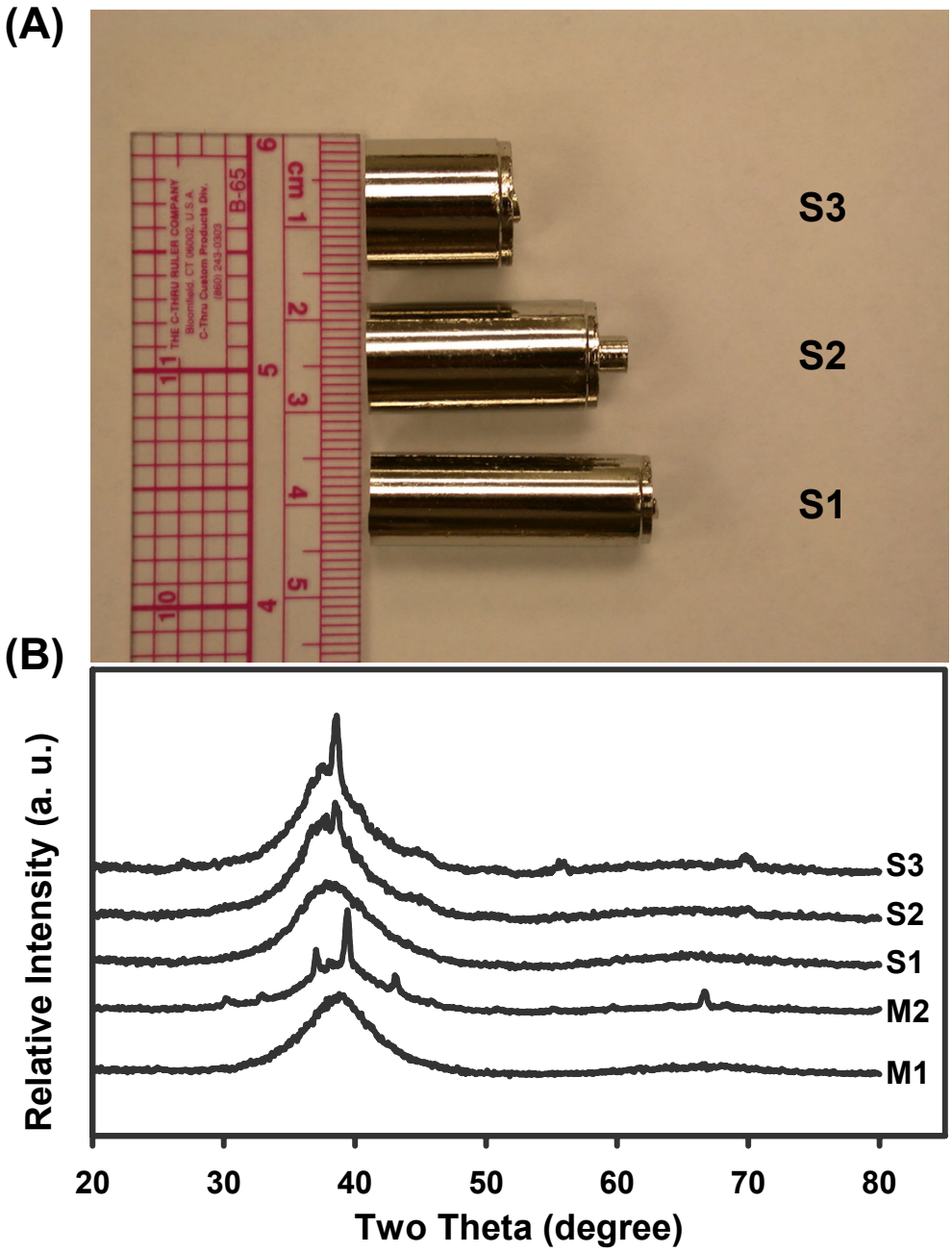

Fig 5.1 (A) Pictures of three cast samples of $Cu_{46}Zr_{42}Al_7Y_5$ with different diameters: S1, 10mm; S2, 12mm; S3, 14mm; (B) XRD patterns obtained from 10mm (S1), 12mm (S2) and 14mm (S3) diameter rods of $Cu_{46}Zr_{42}Al_7Y_5$, and from 3mm (M1) and 4mm (M2) diameter rods of the matrix alloy, $Cu_{46}Zr_{47}Al_7$

the critical casting diameter of the matrix alloy is only ~3mm -- in agreement with the report in Ref. [4].

Table 5.1 lists some representative alloys studied in this work, together with their selected properties. The T_g and T_x values in the table were obtained from the DSC scans which are shown in Fig 5.2. These alloys all exhibit a clear endothermic glass transition, followed by a series of exothermic events characteristic of crystallization. As Y content increases, the exothermic peaks tend to be broadened, indicating a possible slowdown in the kinetics of nucleation and growth.

Table 5.1 A list of representative alloys and selected properties

Alloy Composition (in at.%)	Critical casting diameter (mm)	T_g (K)	T_x (K)	T_l (K)	$\Delta T = T_x - T_g$ (K)	$T_{rg} = T_g/T_l$
$Cu_{46}Zr_{54}$	2	696	746	1201	50	0.58
$Cu_{46}Zr_{47}Al_7$	3	705	781	1163	76	0.61
$Cu_{46}Zr_{45}Al_7Y_2$	8	693	770	1143	77	0.61
$Cu_{46}Zr_{42}Al_7Y_5$	10	672	772	1113	100	0.60
$Cu_{46}Zr_{37}Al_7Y_{10}$	4	665	743	1118	78	0.59

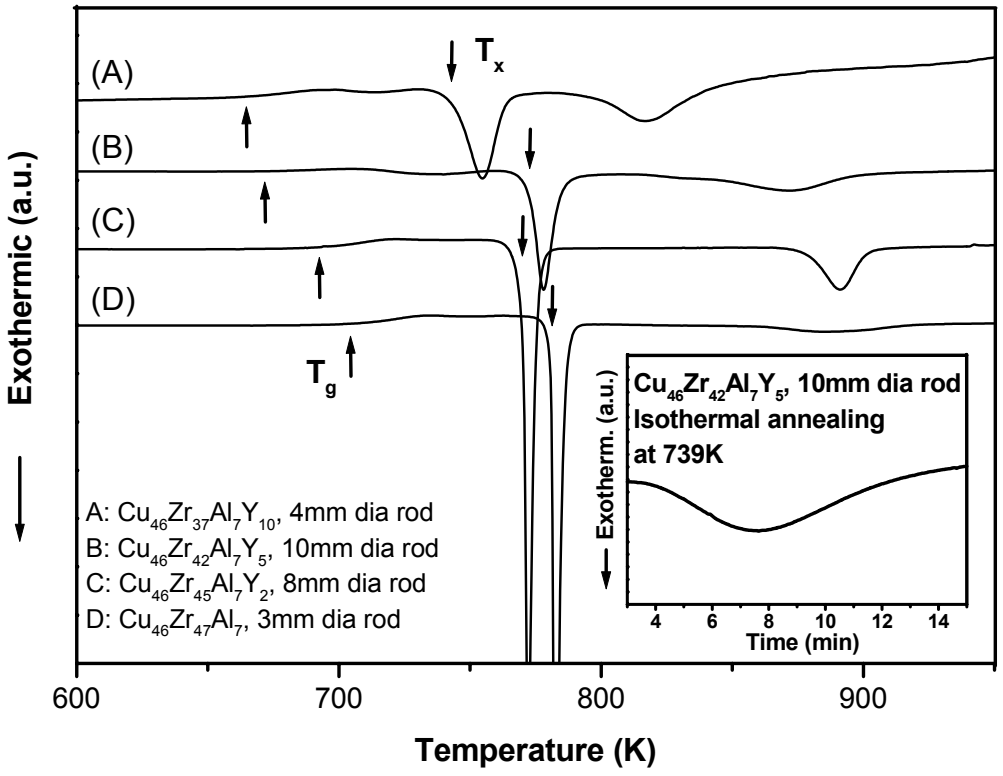

Fig 5.2 DSC scans of selected alloys at a constant heating rate of 0.33K/s. The upward arrows refer to the glass transition temperatures and the downward arrows refer to the onset of the first crystallization events. The inset at the lower right corner is the isothermal DSC profile of the 10mm diameter rod of $Cu_{46}Zr_{42}Al_7Y_5$ at a constant temperature of 739K.

It was pointed out by Chen and Spaepen [6] that isothermal calorimetric profiles can distinguish truly amorphous materials from 'microcrystalline' materials that exhibit similarly broad diffraction halos. Truly amorphous materials exhibit exothermic peaks during isothermal scan, while 'microcrystalline' materials release monotonically decaying heat flow signals. Hence, isothermal scanning was also performed on the present alloys. The inset in Fig 5.2 represents the isothermal DSC profile of the 10mm diameter as-cast sample of $Cu_{46}Zr_{42}Al_7Y_5$ annealed at a constant temperature of 739K. The apparent exothermic peak characteristic of a nucleation-and-growth process confirms the as-cast glassy structure of the alloy as concluded from X-ray diffraction.

In Ref. [3], Lu et al. reported the twofold effect of Y on the glass formation of Fe-based alloys: 1). 'Y adjusted the compositions closer to the eutectic, and thus, lowered their liquidus temperatures'; 2). 'Y improved the manufacturability of these alloys by scavenging the oxygen impurity from it via the formation of innocuous yttrium oxides.' Before discussing other contributing factors, we first confirm whether this 'twofold effect' of Y also applies to the present Cu-based alloys.

The melting behaviors of these alloys were studied through high temperature calorimetric scanning. The signals are exhibited in Fig 5.3, where the liquidus temperatures, T_l (defined by the offset temperature of an entire melting process) are marked with arrows, whose values are included in Table I. It can be seen that Y content significantly affects T_l and the melting behaviors of these alloys. The ternary matrix alloy, $Cu_{46}Zr_{47}Al_7$ has a rather high T_l ~1163 K, although it is quite close to a ternary eutectic composition, as indicated by the nearly-single event feature of its melting process (the ternary eutectic is

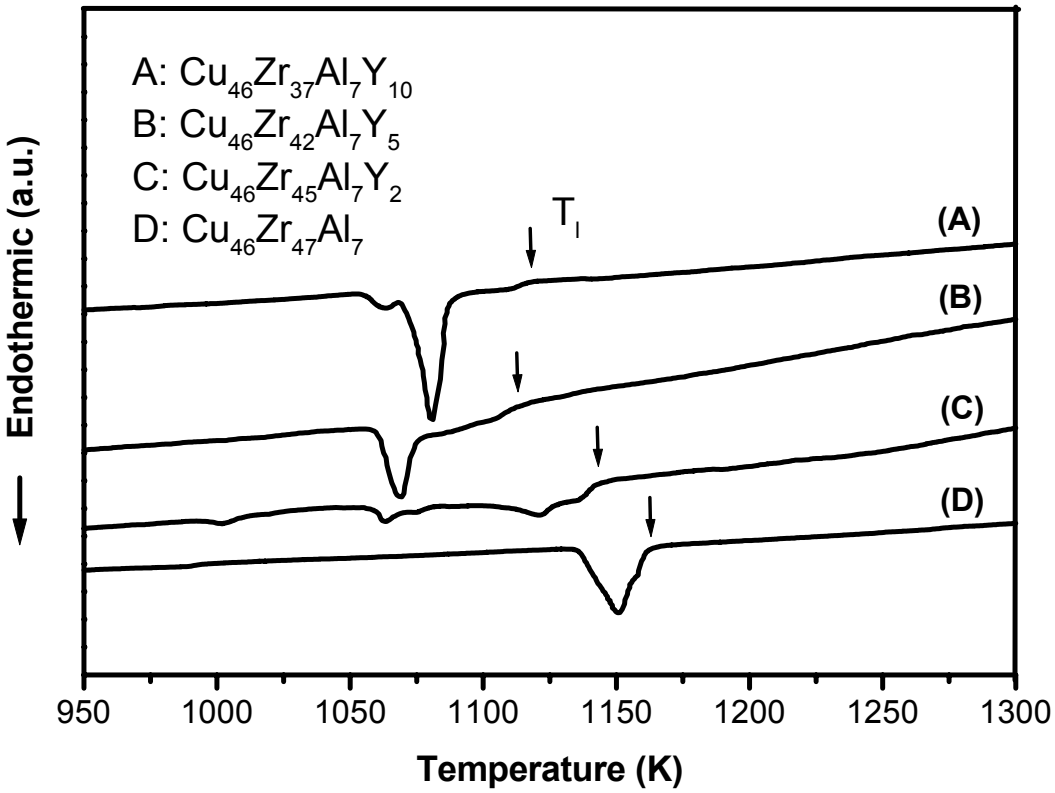

Fig 5.3 Melting behaviors of selected alloys measured at a heating rate of 0.33K/s. The arrows refer to the liquidus temperatures.

located around $Zr_{50}Cu_{40}Al_{10}$ according to Ref. [8]). When 2% Y is added, the quaternary alloy, $Cu_{46}Zr_{45}Al_7Y_2$ shows a lower T_l (~1143 K), but multiple exothermic events which indicate that this alloy is quite far from any quaternary eutectic composition. With 5% Y, the alloy, $Cu_{46}Zr_{42}Al_7Y_5$ shows an even lower T_l (~1113 K) and a simpler melting process consisted of one major exothermic event characteristic of a quaternary eutectic reaction, followed by a minor secondary event corresponding to the melting of a less-concentrated primary crystal. When Y content is further increased, the T_l tends to become higher, reaching ~1118 K at 10% Y, and multiple events appear again during its melting process. It is apparent that the alloy, $Cu_{46}Zr_{42}Al_7Y_5$ which has the highest GFA is the closest to a nearby quaternary eutectic among this present alloy series.

Considering together $Cu_{46}Zr_{54}$, $Cu_{46}Zr_{47}Al_7$, and the present $Cu_{46}Zr_{42}Al_7Y_5$, one can find that all three of these bulk glass-formers are associated with, although not exactly at, the eutectic compositions in their individual systems (binary, ternary and quaternary, respectively). As the dimension of the alloy system (i.e., the number of components) increases, the eutectic temperature is continuously lowered, and the GFA of the alloys is improved as evidenced by the increased critical casting thickness using the same copper mold casting method (refer to Table 5.1). This agrees with the 'confusion principle' proposed in Ref. [9] and the previous observation that high GFA often occurs around deep eutectics [10]. Therefore, it is clear that the unusual GFA of the present quaternary alloy series -- especially the alloy $Cu_{46}Zr_{42}Al_7Y_5$ – comes, in part, from the alloying effect of Y which lowers the liquidus temperature of the matrix alloy and brings the composition to a deeper eutectic.

To study the possible effect of Y on the oxygen impurities and examine the microstructures of the as-cast alloys, TEM, EDS and X-ray dot mapping techniques were utilized. Fig 5.4(a) presents the TEM image obtained from a typical area of the ultra-microtomed section of as-cast $Cu_{46}Zr_{42}Al_7Y_5$ alloy. It can be seen that there are some small particles dispersed in a broad matrix. SAD (Selected Area Diffraction) shows the matrix is amorphous and exhibits only a set of diffuse halo rings -- in agreement with previous X-ray diffraction and thermal analyses. EDS and X-ray dot mapping show that the small particles in the matrix are mainly composed of Y and oxygen. Fig 5.4(b) and (c) represent as two examples the Cu Kα1 and Y Kα1 X-ray dot map images, respectively. Zr and Al map images resemble the Cu map image; all three of these appear very dark across the small particles, but appear bright in the matrix, indicating that the particles are much depleted of Cu, Zr and Al. In contrast, the Y and O map images are very similar, both showing greater brightness across the particles than in the matrix, thus indicating that Y and O are the predominant constituent elements of the small particles.

According to the law of mass action in thermodynamics, the concentration of the dissolved oxygen, [*O*], in the matrix upon the establishment of the following equilibrium: $xM + O \leftrightarrow M_xO$ (*M* refers to a metal; *O*, oxygen; *x* may be either a fraction or an integer), is proportional to $\exp(\frac{\Delta G_f}{RT})$, where ΔG_f is the normalized Gibbs energy of formation of oxide M_xO. Given $\Delta G_f = \Delta H_f - T\Delta S_f$ (where ΔH_f and ΔS_f are the normalized enthalpy and entropy of formation of M_xO, respectively), one gets

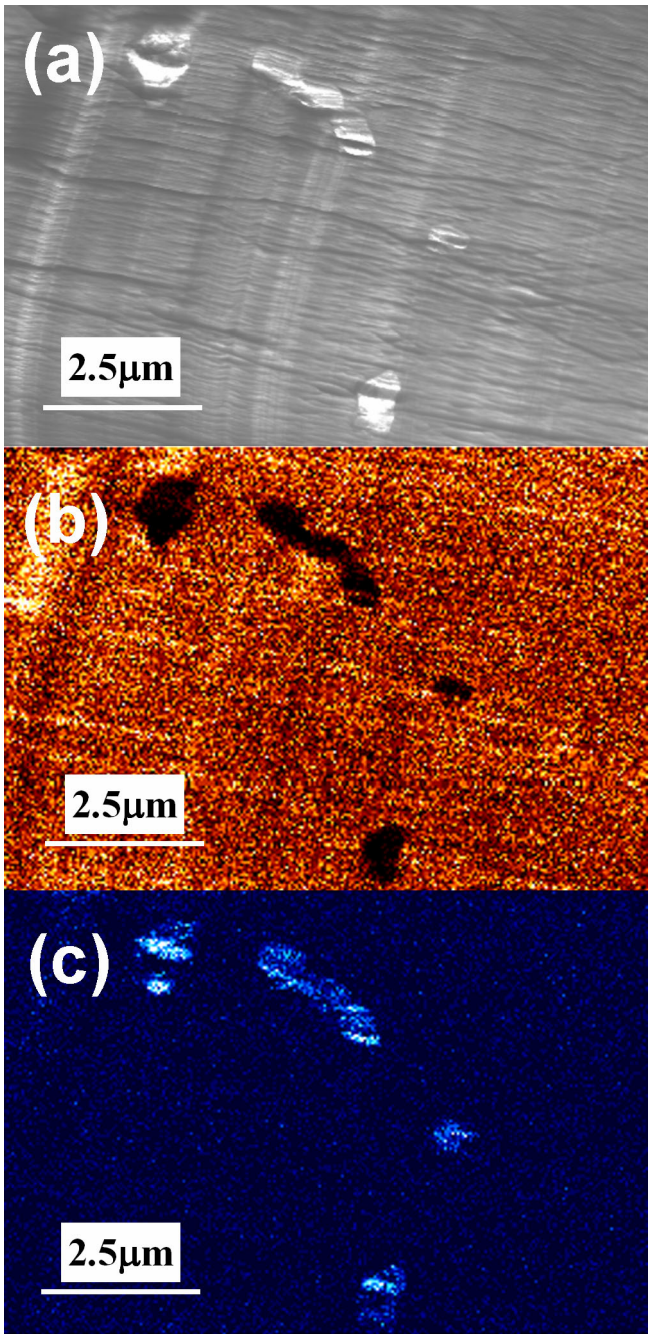

Fig 5.4 TEM image (a), Cu Kα1 X-ray dot map image (b) and Y Kα1 X-ray dot map image (c), of as-cast $Cu_{46}Zr_{42}Al_7Y_5$. The ripples and scratches in the images were caused by the ultramicrotomy sample preparation method.

$[O] \propto \exp(\frac{\Delta H_f}{RT} - \frac{\Delta S_f}{R})$. In the present concerned temperature range (several hundred Kelvin) and in the present alloy system, we have $\left|\frac{\Delta H_f}{RT}\right| \rangle\rangle \frac{\Delta S_f}{R}$ [11]. Therefore, larger negative values of ΔH_f will result in lower [O]. The normalized values of ΔH_f (corresponding to one mole of O atoms) for ZrO_2, CuO, Al_2O_3, and Y_2O_3 are: -550.3, -157.3, -558.6, -635.1 kJ/mol [11], respectively. One can see that Y oxide has a very large negative value of ΔH_f, highest among all the four oxides. On one hand, by forming Y oxide, the addition of Y to the matrix alloy can significantly lower the concentration of oxygen dissolved in the matrix. On the other hand, it also greatly reduces the number of oxygen atoms bonding with Zr, Cu and Al. Since Y oxides are 'innocuous' particles and do not actively trigger heterogeneous nucleation [3], this change in the state of presence of oxygen leads to an enhanced GFA.

Besides the above confirmed 'twofold effect' of Y, the particularly large GFA of the present Cu-based alloys may have benefited from other factors. The present quaternary alloys can be considered as close derivatives from a simple binary base alloy, $Cu_{46}Zr_{54}$ (reported in Chapter 3). The subsequent additions of Al and Y follow the 'confusion principle' proposed by Greer [9]. The more uniformly distributed atomic sizes (Y: 1.8 Å; Zr: 1.6 Å; Al: 1.43 Å; and Cu: 1.28 Å [12]) and the large negative heat of mixing among the constituent elements (e.g., Y-Al: -31 kJ/mol; Y-Cu: -22 kJ/mol; and Zr-Cu: -23 kJ/mol [13]) help stabilize the supercooled liquids and thus, lead to a high GFA [7].

5.4 Conclusions

Unusual glass-forming ability of a family of Cu-based alloys ($Cu_{46}Zr_{47-x}Al_7Y_x$ ($0 \leq x \leq 10$)) has been discovered. By injection mold casting, the amorphous structure of a representative alloy, $Cu_{46}Zr_{42}Al_7Y_5$, can be readily obtained with a diameter above 1cm. By using high temperature thermal analysis, TEM, EDS and X-ray dot mapping techniques, the achievement of such an unusual GFA was found to be associated with the 'twofold effect' of Y as previously reported for Fe-based amorphous alloys [3]. Meanwhile, a bulk glass-forming binary alloy, $Cu_{46}Zr_{54}$, has provided an excellent basis for the extraordinary success of Y-doping and the 'confusion principle' [9] in this particular system.

References

[1] X. H. Lin, W. L. Johnson and W. K. Rhim, Mater. Trans., JIM **38**, 473 (1997).

[2] A. J. Drehman and A. L. Greer, Acta Metall. **32**, 323 (1984).

[3] Z. P. Lu, C. T. Liu and W. D. Porter, Appl. Phys. Lett. **83**, 2581 (2003).

[4] A. Inoue and W. Zhang, Mater. Trans. **43**, 2921 (2002).

[5] D. H. Xu, G. Duan and W. L. Johnson, Phys. Rev. Lett. **92**, 245504 (2004).

[6] L. C. Chen and F. Spaepen, Nature **336**, 366 (1988).

[7] A. Inoue, Acta Mater. **48**, 279 (2000).

[8] Y. Yokoyama, H. Inoue, K. Fukaura and A. Inoue, Mater. Trans. **43**, 575 (2002).

[9] A. L. Greer, Nature **366**, 303 (1993).

[10] W. L. Johnson, Mater. Sci. Forum **225**, 35 (1996).

[11] D. R. Lide, *Handbook of Chemistry and Physics*, 81st ed. (CRC Press, Boca Raton, 2000).

[12] C. Kittel, *Introduction to Solid State Physics*, 7th ed. (John Wiley & Sons, New York, 1996).

[13] F. R. de Boer, R. Boom, W. C. M. Matterns, A. R. Miedema and A. K. Niessen, *Cohesion in Metals* (North-Holland, Amsterdam, 1988).

Chapter 6

Concluding Remarks

During this thesis research, my interest was mainly focused on the development of novel bulk metallic glasses based on ordinary metals, particularly nickel and copper. For me, alloy development is a tempting job that provides excitement once in a while, although it can be quite boring between periods of those exciting moments. To find really useful materials is not an easy job. Although there are several 'wise' rules proposed about how to find BMG alloys (some of them discussed in Chapter 1), the most important factors for success in alloy development are perhaps hard work and persistent interest.

Are the materials developed in this thesis useful? Yes, but only to some extent. They are useful in the following sense: 1. $Ni_xCu_{a-x}Ti_yZr_{b-y}Al_{10}$ (a~b~45, in at.%) (see Chapter 2) alloys are quite strong, having fracture strength (compressive) of ~2.2 - 2.4 GPa, Young's modulus of >110 GPa, Vicker's hardness of >800 Kg/ mm^2 and yet, not too brittle (with no premature failure), together with fairly good glass-forming ability (up to 5 mm in critical casting thickness -- the highest value achieved so far for nickel based BMGs); 2. $Cu_{46}Zr_{54}$, $Cu_{64}Zr_{36}$, $Cu_{66}Hf_{34}$ and other binary BMGs in Cu-Zr and Cu-Hf systems are so far, perhaps the best combination of good glass-forming ability and chemical simplicity which should qualify them as very good subjects for theoretical simulation and modeling; they are also interesting for their own properties: the two rich in copper are quite strong and the one rich in zirconium is quite ductile; 3. $Cu_{46}Zr_{47-x}Al_7Y_x$ ($0<x<10$) are the best glass-formers based on cheap metal copper with a critical casting thickness up to 1 cm. They are, at the same time, not extremely useful in the sense

that: 1. $Ni_xCu_{a-x}Ti_yZr_{b-y}Al_{10}$ (a~b~45, in at.%) and the binary BMGs in Cu-Zr and Cu-Hf systems are still limited in glass forming ability; 2. $Cu_{46}Zr_{47-x}Al_7Y_x$ ($0<x<10$) alloys, although very good glass-formers, are not significantly different from early Zr-based BMGs in terms of material costs and strength.

Finally, I would like to conclude this thesis with a very important thought: “Nothing should be taken for granted in scientific research.” This has led me to the discovery of binary bulk metallic glasses and should continue to benefit me in my academic career in the future.